

MILLIMETER OBSERVATIONS OF CS, HCO⁺, AND CO TOWARD FIVE PLANETARY NEBULAE: FOLLOWING MOLECULAR ABUNDANCES WITH NEBULAR AGE

J. L. EDWARDS¹, E. G. COX^{2,3}, AND L. M. ZIURYS^{1,2}

¹ Department of Chemistry, The University of Arizona, P.O. Box 210041, Tucson, AZ 85721, USA; lziurys@email.arizona.edu

² Department of Astronomy and Steward Observatory, Arizona Radio Observatory, The University of Arizona, 933 North Cherry Avenue, Tucson, AZ 85721, USA
Received 2014 March 24; accepted 2014 July 2; published 2014 July 29

ABSTRACT

Millimeter and sub-millimeter observations of CO, CS, and HCO⁺ have been conducted toward five planetary nebulae (PNe: K4-47, NGC 6537 (Red Spider), M2-48, NGC 6720 (Ring), and NGC 6853 (Dumbbell)), spanning an age range of 900–10,000 yr, using the Sub-Millimeter Telescope and the 12 m antenna of the Arizona Radio Observatory. The $J = 5 \rightarrow 4$, $J = 3 \rightarrow 2$, and $J = 2 \rightarrow 1$ transitions of CS at 245, 147, and 98 GHz, as well as the $J = 3 \rightarrow 2$ and $J = 1 \rightarrow 0$ lines of HCO⁺ at 268 and 89 GHz, were detected toward each source. At least three rotational transitions of CO have also been observed, including the $J = 6 \rightarrow 5$ and $J = 4 \rightarrow 3$ lines at 691 and 461 GHz. CS had not been definitively identified previously in PNe, and new detections of HCO⁺ were made in four of the five nebulae. From a radiative transfer analysis of the CO and CS data, kinetic temperatures of $T_K \sim 10\text{--}80$ K and gas densities of $n(\text{H}_2) \sim 0.1\text{--}1 \times 10^6 \text{ cm}^{-3}$ were determined for the molecular material in these sources. Column densities for CO, CS, and HCO⁺ were $N_{\text{tot}} \sim 0.2\text{--}5 \times 10^{16} \text{ cm}^{-2}$, $N_{\text{tot}} \sim 0.4\text{--}9 \times 10^{12} \text{ cm}^{-2}$, and $N_{\text{tot}} \sim 0.3\text{--}5 \times 10^{12} \text{ cm}^{-2}$, respectively, with fractional abundances, relative to H₂, of $f \sim 0.4\text{--}2 \times 10^{-4}$, $f \sim 1\text{--}4 \times 10^{-8}$, and $f \sim 1 \times 10^{-8}$, with the exception of M2-48, which had $f(\text{HCO}^+) \sim 10^{-7}$. Overall, the molecular abundances do not significantly vary over a duration of 10,000 yr, in contrast to predictions of chemical models. The abundances reflect the remnant asymptotic giant branch shell material, coupled with photochemistry in the early PN phase. These observations also suggest that PNe eject substantial amounts of molecular material into the diffuse interstellar medium.

Key words: astrochemistry – ISM: molecules – planetary nebulae: individual (K4-47, M2-48, NGC 6537, NGC 6720, NGC 6853) – radio lines: ISM

Online-only material: color figures

1. INTRODUCTION

The majority of stars ($M_* \sim 0.5\text{--}8 M_\odot$) in the Galaxy will become planetary nebulae (PNe) at the end of their life cycle. Following the asymptotic giant branch (AGB), such stars pass through the proto-planetary nebula (PPN) phase and then evolve into PNe, characterized by bright optical emission lines with a hot, UV-emitting central white dwarf surrounded by the remnant AGB shell (e.g., Kwok 2000). The progenitor AGB shells are rich molecular factories, and a significant amount of this molecular material survives through the PPN stage and into the PN phase (e.g., Pardo et al. 2007; Bachiller et al. 1997; Zhang et al. 2008; Tenenbaum et al. 2009). Surveys of CO by Huggins and collaborators (e.g., Huggins et al. 1996, 2005), for example, have found this molecule in numerous PNe. Perhaps more interesting, observations by Bachiller et al. (1997) and Josselin & Bachiller (2003) have identified CN, HCN, HNC, and HCO⁺ in several such nebulae. A survey of the very young PN NGC 7027 by Zhang et al. (2008) showed the presence of CO, CN, CCH, HCN, HCO⁺, HC₃N, N₂H⁺, and possibly C₃H₂ in this object, but a lack of CS and HNC, while Liu et al. (1996) found OH, CH, CH⁺, and CO⁺ in this source, as well. In the oldest PN known, the Helix Nebula, CN, HCN, HNC, HCO⁺, H₂CO, C₃H₂, and CCH have been detected (Bachiller et al. 1997; Tenenbaum et al. 2009). While these observations focused on one position in this large, roughly 1000'' diameter source, large-scale mapping observations have shown that both HCO⁺ and H₂CO are widespread throughout the nebula (Zack

& Ziurys 2013; Zeigler et al. 2013). Furthermore, a very recent molecular study of the high excitation Red Spider Nebula (NGC 6537) identified CN, HCN, HNC, CCH, CS, SO, H₂CO, HCO⁺, and N₂H⁺ in this object (Edwards & Ziurys 2013). These observations suggest that PNe, even the very evolved ones, have a significant molecular component.

A comparison of the Helix, the Red Spider, and NGC 7027 suggest that molecular abundances in PNe are not governed by nebular age (Edwards & Ziurys 2013; Zack & Ziurys 2013). The molecular content of PNe remains high even in the final stages, a result of self-shielding clumps that limit the extent of photodissociation. Thus, molecular material may be seeding the diffuse interstellar medium (ISM), and at a substantial rate. Over 85% of interstellar matter comes from PNe (e.g., Dorschner & Henning 1995). Chemical models of PNe, on the other hand, suggest that their molecular content decreases significantly with time, due to the extreme UV radiation emitted from the central star (e.g., Ali et al. 2001; Redman et al. 2003; Kimura et al. 2012). For example, Redman et al. (2003) predict the abundance of HCO⁺ to drop from $f(\text{HCO}^+/\text{H}_2) \sim 1 \times 10^{-10}$ at 2500 yr to $\sim 6 \times 10^{-12}$ at 10,500 yr, while that of HCN decreases steadily from 4×10^{-5} to 1×10^{-12} over the same time interval. The abundance of CS falls by a factor of 1000 over this time, as well, from 10^{-5} to 10^{-8} . Only CO appears to escape this general fate.

In order to further elucidate the chemical content of PNe and its dependence on age, we have conducted multiline observations of CS and HCO⁺ in five PNe of varying age from ~ 1000 to 10,000 yr. All sources were known to have relatively strong CO and ¹³CO emission, based on previous surveys and Arizona Radio Observatory (ARO) observations. HCO⁺ is of interest because it is a high density tracer, and has been already

³ Current Address: Department of Astronomy, The University of Illinois at Urbana-Champaign, 1002 West Green Street, Urbana, IL 61801, USA.

Table 1
Properties of Observed Planetary Nebulae

Source	α (J2000.0)	δ (J2000.0)	T_* (10^5 K)	Age (yr)	Size	Morphology	C/O	$N(\text{H}_2)$ (cm^{-2})
K4-47	04 ^h 20 ^m 45 ^s .2	56° 18' 12".1	1.15–1.3 ^a	900 ⁺³⁰⁰ ₋₅₀₀ ^b	10 ^{''c}	Bipolar? ^b	...	2.9×10^{20} ^d
NGC 6537	18 ^h 05 ^m 13 ^s .1	−19° 50' 34".9	3.4 ^e	1,600 ^{+1,000} ₋₅₀₀ ^e	30 ^{''f}	Bipolar ^f	0.95 ^g	2.3×10^{20} ^h
M2-48	19 ^h 50 ^m 28 ^s .5	25° 54' 29".5	...	4,800 ^{+4,000} _{-3,000} ⁱ	30'' × 20 ^{''j}	Bipolar ^j	...	4.5×10^{19} ^k
NGC 6720	18 ^h 53 ^m 35 ^s .1	33° 01' 45".0	1.2–1.6 ^l	7,000 ^{+4,500} _{-2,000} ^l	~100 ^{''m}	Bipolar ^l	0.7–0.9 ⁿ	2.7×10^{19} ^m
NGC 6853	19 ^h 59 ^m 32 ^s .1 ^o	23° 42' 13".0 ^o	1.2 ^p	10,000 ^{+1,900} _{-1,300} ^q	8' × 11 ^{''r}	Bipolar/multipolar? ^s	0.72 ^t	2.9×10^{19} ^u

Notes.

^a Gonçalves et al. (2004).

^b Corradi et al. (2000) and Gonçalves et al. (2004); see the text for details.

^c Saito et al. (1999).

^d Kastner et al. (1996), assumes $T_{\text{ex}}(\text{H}_2) \sim 1550$ K from Lumsden et al. (2001).

^e Matsuura et al. (2005).

^f Cuesta et al. (1995).

^g Pottasch et al. (2000).

^h Davis et al. (2003), assumes $T_{\text{ex}}(\text{H}_2) \sim 1200$ K from Lumsden et al. (2001).

ⁱ Dobrinčić et al. (2008).

^j Vázquez et al. (2000).

^k Derived assuming $\text{CO}/\text{H}_2 \sim 10^{-4}$ (see the text).

^l O'Dell et al. (2007).

^m Speck et al. (2003), assumes $T_{\text{ex}}(\text{H}_2) \sim 900$ K based on Cox et al. (1998).

ⁿ Liu et al. (2004).

^o Offset (−68", −63") from central position $\alpha = 19^{\text{h}}59^{\text{m}}36^{\text{s}}.4$; $\delta = 23^{\circ}43'15''.8$ (J2000.0)

^p Rauch (2003).

^q O'Dell et al. (2002).

^r Papamastorakis et al. (1993).

^s Kwok et al. (2008).

^t Pottasch et al. (1982).

^u S. Baldrige et al. (in preparation), assumes $T_{\text{ex}}(\text{H}_2) \sim 900$ K based on Cox et al. (1998).

observed in a number of PNe, as mentioned. CS, in contrast, has been surprisingly absent in PNe (e.g., Bachiller et al. 1997; Zhang et al. 2008), other than the Edwards & Ziurys (2013) work on the Red Spider and the observation of one line of this molecule in IC4406 (Woods & Nyman 2005); however, it is common in both C-rich and O-rich circumstellar envelopes and in PPNe (e.g., Tenenbaum et al. 2010; Pardo et al. 2007). In this paper we present our observations and their analysis, and discuss the implications for the chemistry and morphology of these nebulae.

2. OBSERVATIONS

The measurements were conducted between 2009 December and 2013 March using the telescopes of the Arizona Radio Observatory (ARO). The observations at 2 and 3 mm were made using the ARO 12 m at Kitt Peak, AZ. The receiver at 2 mm consisted of dual polarization, single-sideband SIS mixers with image rejections typically >16 dB, achieved by tuning of the mixer backshorts. Measurements at 3 mm were made using a dual polarization receiver equipped with ALMA Band 3 sideband-separating (SBS) mixers with image rejection ≥ 18 dB, intrinsic in the mixer architecture. The backends employed were two 256 channel filter banks with either 500 kHz, 1 MHz, or 2 MHz resolutions configured in parallel mode (2×128 channels) to accommodate both receiver polarizations. The temperature scale T_R^* was determined by the chopper-wheel method, corrected for forward spillover losses, where $T_R = T_R^*/\eta_c$ and η_c is the corrected beam efficiency and T_R is the main beam brightness temperature.

Measurements at 1 mm, 0.8 mm, 0.7 mm, and 0.4 mm were made using the ARO 10 m Sub-Millimeter Telescope (SMT) on

Mt. Graham, AZ. All receivers were dual polarization except the 0.7 mm system. The 1 mm receiver utilizes ALMA Band 6 SBS SIS mixers, with image rejection typically >18 dB, while that at 0.8 mm consists of dual polarization, double-sideband (DSB) SIS mixers. The 0.4 mm receiver consists of ALMA Band 9 DSB mixers, while the instrument at 0.7 mm employs a new ALMA-type Band 8 SBS SIS mixer, developed jointly by ARO and NRAO. Here image rejection was typically 15–20 dB. The temperature scale at the SMT is T_A^* , determined by the chopper wheel method, where $T_R = T_A^*/\eta_b$, and η_b is the main beam efficiency. The backend used was a 2048-channel 1 MHz resolution filter bank configured in parallel mode (2×1024 channels).

Given their respective source sizes, K4-47 and M2-48 were observed in beam-switching mode with a beam throw of $\pm 2'$. For the other objects, position-switching mode was employed with an azimuth offsets of 5' for NGC 6537 and NGC 6720 and 15' for NGC 6853. Local oscillator shifts were done to test for image contamination. Pointing and focus were determined using planets or strong continuum sources. Source properties including age, assumed source size, basic morphology, C/O ratio, and H_2 column density, along with observing coordinates, are given in Table 1. Observing frequencies, beam efficiencies, and beam sizes are provided in Table 2.

3. RESULTS

3.1. Overview of the Data Set

Figures 1(a)–5(a) contain optical images of the PNe studied, overlaid with the smallest (in red) and largest (in blue) beam

Table 2
Observed Molecular Transitions^a

Molecule	Transition	Telescope	ν (MHz)	η_b or η_c	θ_b ($''$)
CO	$J = 6 \rightarrow 5$	SMT	691473.1	0.60	11
	$J = 4 \rightarrow 3$	SMT	461040.8	0.62	16
	$J = 3 \rightarrow 2$	SMT	345796.0	0.66	22
	$J = 2 \rightarrow 1$	SMT	230538.0	0.76	32
	$J = 1 \rightarrow 0$	12 m	115271.2	0.84	54
HCO ⁺	$J = 3 \rightarrow 2$	SMT	267557.6	0.76	28
	$J = 1 \rightarrow 0$	12 m	89188.5	0.89	69
CS	$J = 5 \rightarrow 4$	SMT	244935.6	0.76	30
	$J = 3 \rightarrow 2$	12 m	146969.0	0.75	42
	$J = 2 \rightarrow 1$	12 m	97981.0	0.80	63

Note. ^a Observed with 1 MHz resolution.

sizes observed for each source. Multiple transitions of CO, CS, and HCO⁺ were detected in all five observed PNe, as shown in Figures 1(b)–5(b). These data are the first definitive identifications of CS in PNe, other than a single line detection in IC4406 (Woods & Nyman 2005), and the first detections of HCO⁺ in K4-47, M2-48, NGC 6537, and NGC 6853. HCO⁺ had been previously detected in the NGC 6720 (Ring) via its $J = 1 \rightarrow 0$ transition by Bachiller et al. (1997). The CS and HCO⁺ data in NGC 6537 (Red Spider) have been previously reported in Edwards & Ziurys (2013), along with numerous other molecules. For CS, the $J = 5 \rightarrow 4$, $J = 3 \rightarrow 2$, and $J = 2 \rightarrow 1$ transitions were detected in all five PNe, except for K4-47, where the $J = 2 \rightarrow 1$ line is tentative. Both the $J = 3 \rightarrow 2$ and $J = 1 \rightarrow 0$ transitions of HCO⁺ were identified in all five sources, as well. Three to four transitions of CO were also observed in each nebula, including the higher excitation lines $J = 3 \rightarrow 2$ (all five sources), $J = 4 \rightarrow 3$ (NGC 6537 and M2-48), and $J = 6 \rightarrow 5$ (K4-47, NGC 6537, and M2-48). The $J = 2 \rightarrow 1$ and $J = 1 \rightarrow 0$ transitions of CO had previously been observed in NGC 6720 and NGC 6853, the Ring and the Dumbbell (Huggins & Healy 1986; Bachiller et al. 1989; Huggins et al. 1996); the $J = 2 \rightarrow 1$ line was measured toward K4-47, NGC 6537, and M2-48 by Huggins et al. (2005).

As shown in Figures 1(b)–5(b), several sources exhibit spectra with complex line profiles. A broad plateau appears to be present in higher frequency data for K4-47, while multiple velocity components are seen for the Ring and Dumbbell Nebulae. Absorption features resulting from Galactic contamination appear in the lower energy transitions of mainly CO for most sources, but are typically shifted away from the main line profiles. These unwanted signals were truncated in the figures. (The raw spectra are presented as insets on the upper left corner of the appropriate panel.) However, the only PN in which Galactic contamination significantly affected the line profiles was M2-48. Here the $J = 2 \rightarrow 1$ transition of CO is highly obscured (see Figure 3(b)) and the $J = 1 \rightarrow 0$ line could not be reliably measured.

Each velocity component within a given transition was modeled with a Gaussian function to establish line parameters: line intensity (T_A^* or T_R^*), LSR velocity, the half-power line width ($\Delta V_{1/2}$), and the integrated intensity. The resulting fits for all spectra are given in Table 3. The CO: $J = 2 \rightarrow 1$ and $1 \rightarrow 0$ parameters are consistent with previous observations of Huggins et al. (1996, 2005). Individual sources are discussed below.

3.2. K4-47

Apart from being a target of large radio and infrared surveys, this PN remained virtually unstudied until the optical emission-line observations by Corradi et al. (2000). This study revealed a detailed kinematic structure consisting of a high excitation core, visible in [O III], [N II], and H α , with two bright lobes traced by [N II], [S II], and H α , as seen in Figure 1(a). Here the [N II] image is presented, adopted from Corradi et al. (2000), along with the CO: $J = 6 \rightarrow 5$ beam size. The low ionization lobes are thought to arise from a high-velocity, collimated outflow stemming from the core and may be associated with jets or bullets of gas ejected from the central star. A more recent study of K4-47 by Gonçalves et al. (2004), exploring its elemental content, found the lobe He and N abundances to be typical of Galactic disk PNe (so-called Type I); however, the core appears to be quite oxygen-deficient, as found for Galactic halo PNe (Type IV). A radiative transfer analysis of the lobe emission lines suggests shock excitation. Strong CO emission was subsequently detected in this source by Huggins et al. (2005). Corradi et al. (2000) estimate an age between 400–900 yr for K4-47, based on a distance of 3–7 kpc (derived from the galactic rotation curve), an expansion velocity of 150 km s⁻¹, and the physical separation of the lobes. On the other hand, a distance of 5.9 kpc was determined for K4-47 by Tajitsu & Tamura (1998) from the IRAS flux. If a somewhat higher expansion velocity of 250 km s⁻¹ is used, as suggested by Gonçalves et al. (2004), an age of ~ 1200 yr is derived, in relative agreement. For the purpose of this paper, an age of 900_{-500}^{+300} yr is adopted (see Table 1).

All molecular features detected toward K4-47 (Figure 1(b)) appear near an LSR velocity of -27 km s⁻¹, in agreement with CO (Huggins et al. 2005). The line profiles also vary between the lower and higher energy transitions (or larger versus smaller beam size). A broad ($\Delta V_{1/2} \sim 60$ km s⁻¹), asymmetric plateau-like feature is clearly visible in the $J = 6 \rightarrow 5$ line of CO, as well as in the $J = 3 \rightarrow 2$ transition of HCO⁺. This component is perceptible in the $J = 3 \rightarrow 2$ and $J = 2 \rightarrow 1$ profiles of CO, but the main central feature ($\Delta V_{1/2} \sim 20$ km s⁻¹) dominates these spectra, as it does the lower energy lines of CS and HCO⁺. The broad plateau material may be related to the shocked gas observed by Gonçalves et al. (2004). The CS and HCO⁺ lines observed in K4-47 are relatively weak (≤ 10 mK).

3.3. NGC 6537 (Red Spider Nebula)

This PN, well-studied in the optical and UV regimes, is one of the highest excitation PNe known, as demonstrated by the presence of [Si VI] emission (e.g., Ashley & Hyland 1988; Aller et al. 1999; Pottasch et al. 2000). Both H₂ (Kastner et al. 1996; Davis et al. 2003), and CO have been detected in this object. The “spider” shape (see Figure 2(a)) is principally an artifact of atomic emission lines, but is also vaguely visible in H₂. A recent millimeter-wave study by Edwards & Ziurys (2013) found the Red Spider to have a rich chemical content, as demonstrated by the detection of numerous molecular species, as mentioned. The age of the nebula is estimated to be ~ 1600 yr, derived by assuming an expansion velocity of 18 km s⁻¹ for the inner region and a distance of 1.5 kpc (Matsuura et al. 2005). These authors also suggested the distance could vary as widely as 0.9–2.4 kpc, corresponding to an age range of 1100–2600 yr.

Figure 2(b) presents the transitions of CO, CS, and HCO⁺ observed in the Red Spider. In this PN, CS emission is relatively strong (~ 30 mK), as opposed to the other sources. In addition,

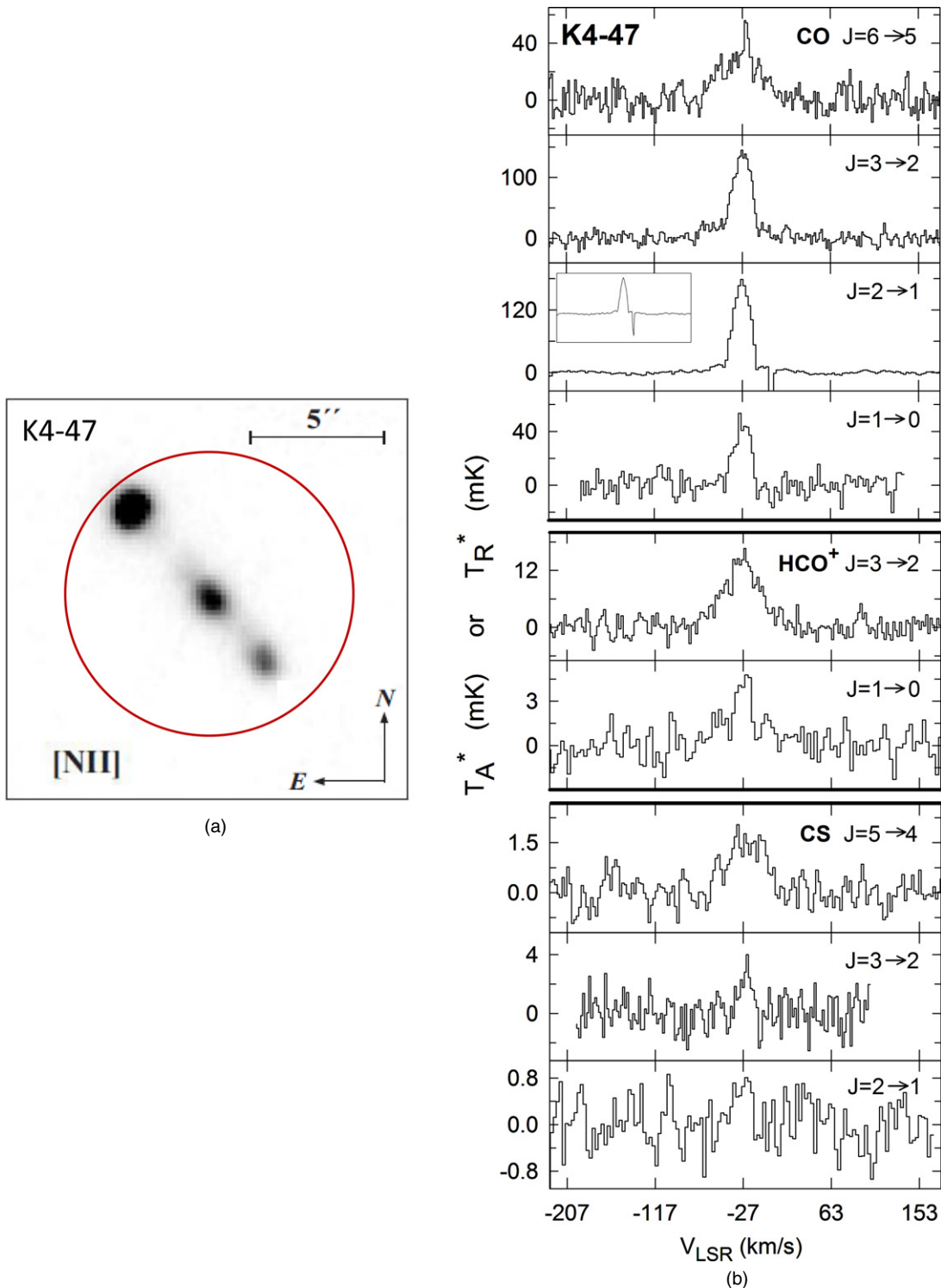


Figure 1. (a) Optical [N II] 6583 Å image of K4-47, adapted from Corradi et al. (2000). The spatial scale is shown in the upper right corner. North and east are indicated in the figure. The smallest beam size used in the observations, for the $J = 6 \rightarrow 5$ transition of CO at 691 GHz ($\theta \sim 11''$), is shown in red. (b) Spectra of CO, HCO⁺, and CS observed toward K4-47. The $J = 6 \rightarrow 5$, $J = 3 \rightarrow 2$, and $J = 2 \rightarrow 1$ transitions of CO, as well as the $J = 3 \rightarrow 2$ transition of HCO⁺ and the $J = 5 \rightarrow 4$ transition of CS, were measured with the ARO SMT (resolution 1 MHz, smoothed to 2 MHz or 4 MHz (CO $J = 6 \rightarrow 5$ line only); temperature scale is T_R^*). The $J = 1 \rightarrow 0$ transitions of CO and HCO⁺ and the $J = 3 \rightarrow 2$ and $J = 2 \rightarrow 1$ transitions of CS were measured using the ARO 12m (1 MHz resolution; temperature scale is T_A^*). The velocity resolution is 1.3–3.3 km s⁻¹. Galactic contamination is present on the redshifted side of the $J = 2 \rightarrow 1$ transition of CO, with the full spectrum inset in the upper left corner of the panel. A broad ($\Delta V_{\text{fwhp}} \sim 90$ km s⁻¹) “plateau”-like feature is present in some spectra, in addition to a central component.

(A color version of this figure is available in the online journal.)

while CS and HCO⁺ display simple, one-component profiles, that of CO is more complex. In the $J = 4 \rightarrow 3$ and $J = 6 \rightarrow 5$ spectra, there is evidence for a blueshifted “shoulder,” a feature observed in HCN and other molecules (Edwards & Ziurys 2013).

A redshifted line wing may also be present in the CO data. Note that the higher frequency observations are coupled to the central region or “body” of the Red Spider, while the 1–3 mm spectra encompass most of the “leg” structures, as well.

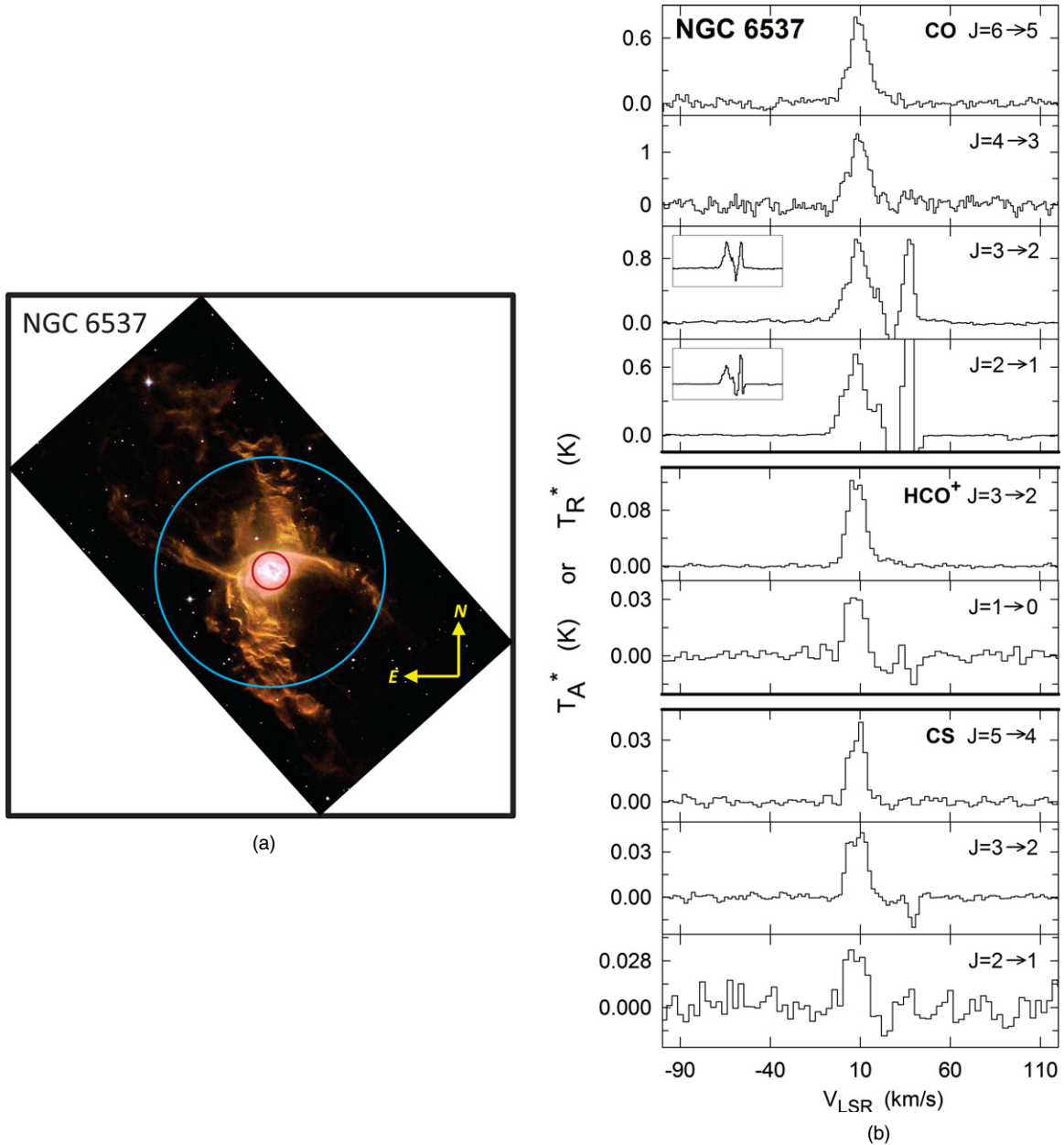


Figure 2. (a) NASA/ESA *Hubble Space Telescope* image of NGC 6537 (Red Spider), a composite of [N II] 6584 Å (red), H α 6563 Å (green), and [O III] 5007 Å (blue) emission. North and east are indicated in the figure. The smallest (11'') and largest (69'') beam sizes, corresponding to the CO: $J = 6 \rightarrow 5$ and HCO $^+$: $J = 1 \rightarrow 0$ transitions, are overlaid on the figure at the observed position, in red and blue. (b) Spectra of CO, HCO $^+$, and CS observed toward NGC 6537. The $J = 6 \rightarrow 5$, $J = 4 \rightarrow 3$, $J = 3 \rightarrow 2$, and $J = 2 \rightarrow 1$ transitions of CO, the $J = 3 \rightarrow 2$ transition of HCO $^+$, and the $J = 5 \rightarrow 4$ transition of CS were measured with the ARO SMT (resolution 1 MHz, smoothed to 2 MHz or 4 MHz (CO $J = 6 \rightarrow 5$ line only); temperature scale is T_A^*). The $J = 1 \rightarrow 0$ transition of HCO $^+$ and the $J = 3 \rightarrow 2$ and $J = 2 \rightarrow 1$ transitions of CS were measured using the ARO 12 m (resolution 1 MHz; temperature is scale T_R^*). Galactic contamination is present near 35 km s $^{-1}$ in the $J = 3 \rightarrow 2$ and $J = 2 \rightarrow 1$ transitions of CO, the $J = 1 \rightarrow 0$ transition of HCO $^+$, and the $J = 3 \rightarrow 2$ and $J = 2 \rightarrow 1$ transitions of CS. Full spectra are inset in the upper left corner of the CO $J = 3 \rightarrow 2$ and $J = 2 \rightarrow 1$ panels.

(A color version of this figure is available in the online journal.)

3.4. M2-48

M2-48 is a middle-aged PN, with an estimated age of $4,800^{+4,000}_{-3,000}$ yr, as determined again from the expansion velocity, size, and distance (Dobrinčić et al. 2008). The uncertainties in the age reflect that in the object's distance, which is not well determined. Optical emission-line studies by Vázquez et al. (2000) and López-Martin et al. (2002) indicate that this nebula has an unusual bipolar structure, consisting of bow-shocked tips extending about $\pm 2'$ from a bright $30'' \times 60''$ core,

with an apparent discontinuity between the two regions (see Figure 3(a), where the bright bow-shocked rims are indicated by pink arrows). The axis of the bipolar flow is $\pm 10^\circ$ relative to the plane of the sky (López-Martin et al. 2002). A fragmented ring $\sim 100''$ in size surrounds the central part of the outflow, likely tracing the remnant AGB shell. Searches for $2 \mu\text{m}$ H $_2$ emission toward M2-48 have failed (Kastner et al. 1996; Sterling & Dinerstein 2008), although Huggins et al. (2005) clearly detected the $J = 2 \rightarrow 1$ transition of CO toward this nebula. More recently, mid-infrared observations of M2-48, conducted

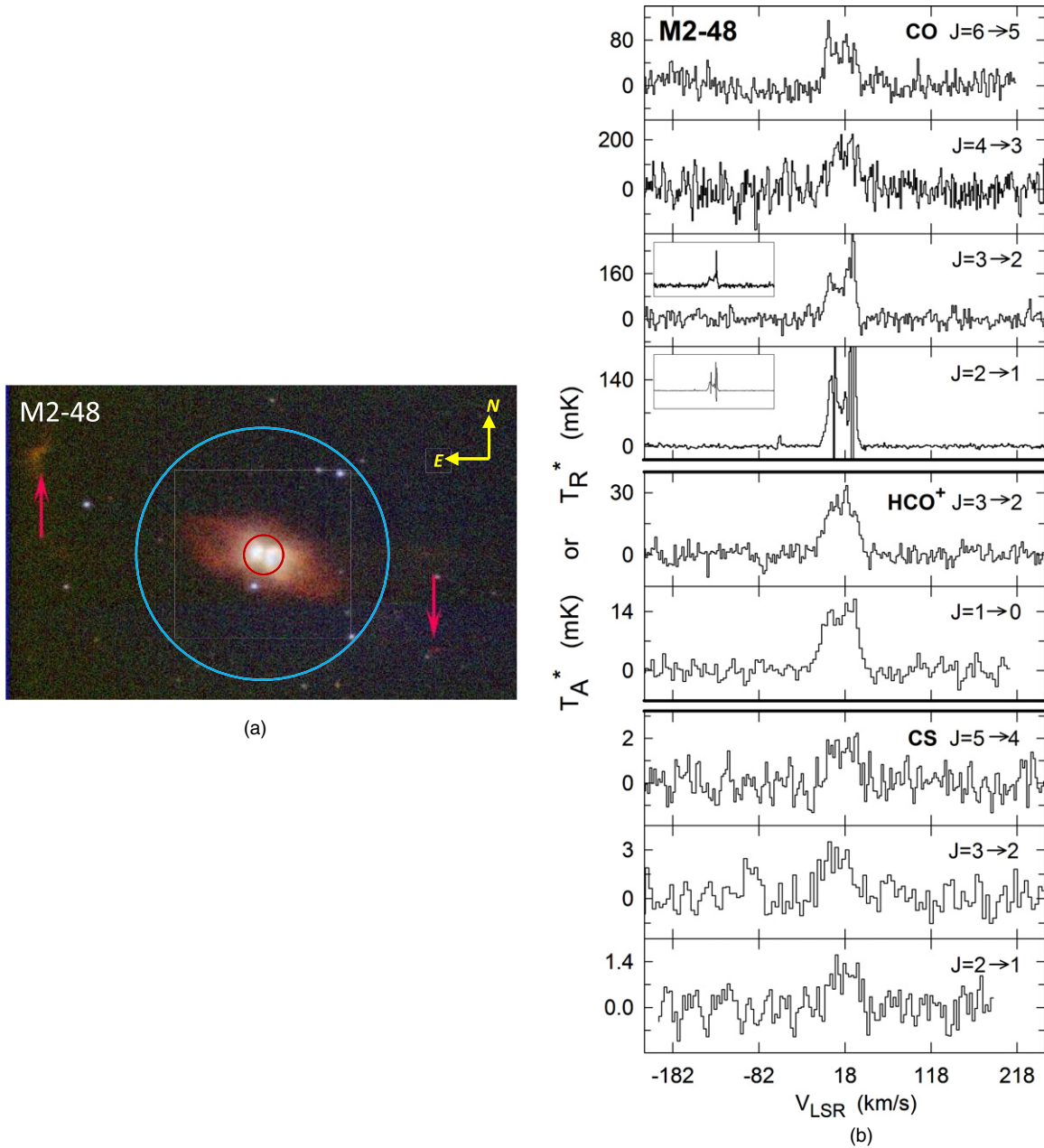


Figure 3. (a) Optical image of M2-48 from the IAC Morphological Catalog of Northern Galactic Planetary Nebulae (Manchado et al. 1996). The red, green, and blue colors indicate [N II] 6584 Å, H α 6563 Å, and [O III] 5007 Å emission, respectively. North and east are indicated in the figure. The smallest (11'') and largest (69'') beam sizes, corresponding to the CO: $J = 6 \rightarrow 5$ and HCO⁺: $J = 1 \rightarrow 0$ transitions, are overlaid on the figure at the observed position, in red and blue. (b) Spectra of CO, HCO⁺, and CS observed toward M2-48. The $J = 6 \rightarrow 5$, $J = 4 \rightarrow 3$, $J = 3 \rightarrow 2$, and $J = 2 \rightarrow 1$ transitions of CO, the $J = 3 \rightarrow 2$ transition of HCO⁺, and the $J = 5 \rightarrow 4$ transition of CS were measured with the ARO SMT (resolution 1 MHz, smoothed to 2 MHz or 4 MHz (CO $J = 6 \rightarrow 5$ line only); temperature scale is T_A^*). The $J = 1 \rightarrow 0$ transition of HCO⁺ and the $J = 3 \rightarrow 2$ and $J = 2 \rightarrow 1$ transitions of CS were measured using the ARO 12 m (resolution 1 MHz; temperature scale is T_R^*). Severe Galactic contamination is present in the $J = 3 \rightarrow 2$ and $J = 2 \rightarrow 1$ transitions of CO with the full spectra inset in the upper left corner of these panels.

(A color version of this figure is available in the online journal.)

by Phillips & Ramos-Larios (2008) with the *Spitzer Space Telescope*, suggest the presence of a dusty collimating disk $\sim 2''$ – $3''$ in extent, oriented perpendicular to the bipolar axis.

As shown in Figure 3(a), the telescope beams used in this work are sufficiently small that they only encompass the central part of the bipolar flow and most of the fragmented ring (not visible), but not the shocked tips. Centered near $V_{\text{LSR}} \sim 15 \text{ km s}^{-1}$, the systemic velocity of the core as traced by [N II] (López-Martin et al. 2002), the line profiles of CO, CS, and HCO⁺ show some evidence of the bipolar structure. The $J = 4 \rightarrow 3$ and $J = 6 \rightarrow 5$ lines of CO sample the inner region of the flow near the proposed

disk, and may display some additional kinematic complexity, although higher signal-to-noise data are clearly needed. The transitions of CS are all very weak (≤ 3 mK).

3.5. NGC 6720 (Ring Nebula)

The Ring, an older PN, has been the object of numerous studies (e.g., O'Dell et al. 2002; van Hoof et al. 2010). The object is thought to be ~ 7000 yr old, based on a kinematical analysis by O'Dell et al. (2007). Uncertainties in the distance suggest a range of 5000–11,500 yr for the age. CO was first

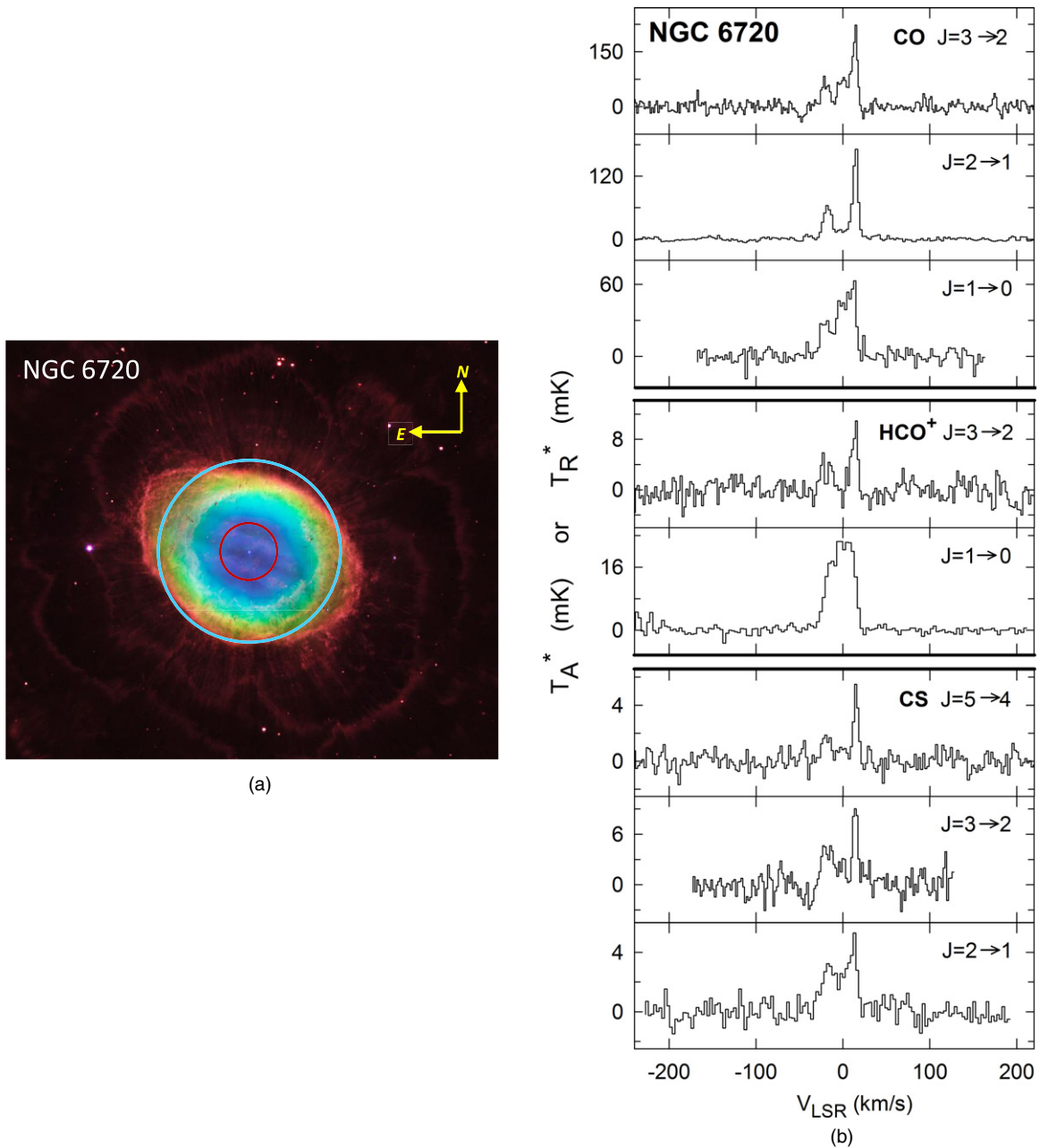


Figure 4. (a) Composite visible and IR image of NGC 6720 from the *Hubble Space Telescope* and the Large Binocular Telescope (O’Dell et al. 2013). North and east are indicated in the figure. The lighter red, green, and blue emission of the main “ring” arises from [N II] 6584 Å, [O III] 5007 Å, and He II 4686 Å, respectively. The faint, more extended dark red emission is due to 2.1 μm H₂ emission. The smallest (22’’) and largest (69’’) beam sizes, corresponding to the CO: $J = 3 \rightarrow 2$ and HCO⁺: $J = 1 \rightarrow 0$ transitions, are overlaid on the figure at the observed position, in red and blue. (b) Spectra of CO, HCO⁺, and CS observed toward NGC 6720. The $J = 3 \rightarrow 2$, and $J = 2 \rightarrow 1$ transitions of CO, the $J = 3 \rightarrow 2$ transition of HCO⁺, and the $J = 5 \rightarrow 4$ transition of CS were measured with the ARO SMT (resolution 1 MHz, smoothed to 2 MHz; temperature scale is T_A^*). The $J = 1 \rightarrow 0$ transitions of CO and HCO⁺, and the $J = 3 \rightarrow 2$ and $J = 2 \rightarrow 1$ transitions of CS were measured using the ARO 12 m (resolution 1 MHz; temperature scale is T_R^*). Red- and blue-shifted velocity components are present in the spectra, with the larger beams sampling material near the systemic velocity of the star (see the text).

(A color version of this figure is available in the online journal.)

observed in this object by Huggins & Healy in 1986, while Zuckerman & Gatley (1988) did the first 2 μm H₂ map of the Ring. Shortly thereafter, Bachiller et al. (1989) mapped both the $J = 2 \rightarrow 1$ and $J = 1 \rightarrow 0$ transitions of CO in this object, finding that the emission of this molecule extended over an 80’’ × 100’’ region. In 2003, Speck et al. reimaged the 2 μm emission of H₂ with 0.65 spatial resolution; their map, which closely resembled that of [N II] emission, suggested H₂ existed in clumpy knots, similar to that observed in the Helix Nebula (e.g., Speck et al.

2002; Meixner et al. 2005; Hora et al. 2006). CN, HCN, HNC, and HCO⁺ have been also observed in the Ring by Bachiller et al. (1997), although they failed to detect CS, HC₃N, SiO, and SiC₂.

As shown in Figure 4(b), there are multiple components present in the molecular line profiles for this object, most clearly seen in the transitions of CO presented in the top three panels. This complexity was also observed in CO by Huggins & Healy (1986) and Bachiller et al. (1989). Such spectra are expected,

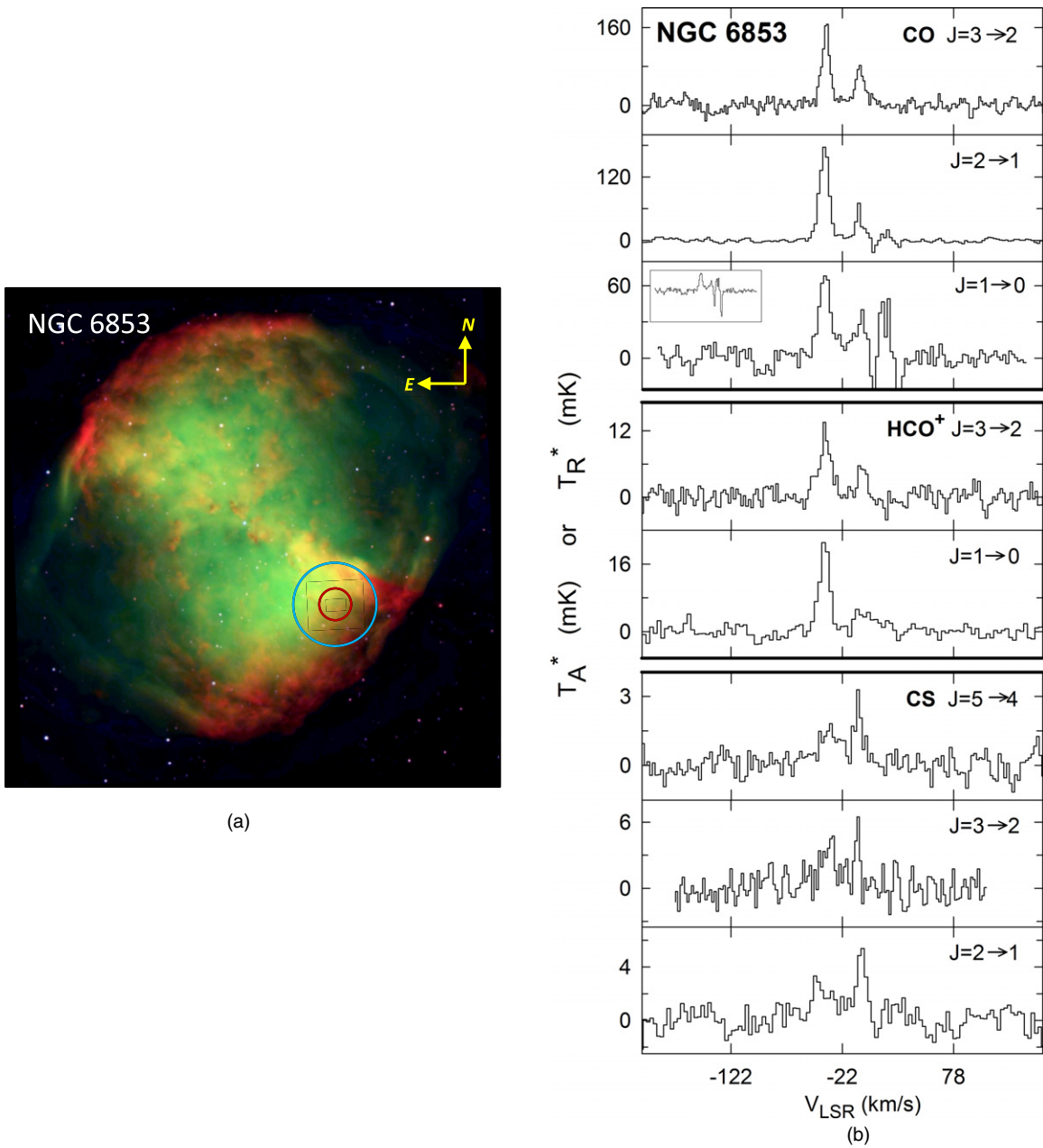


Figure 5. (a) Three-color composite image of NGC 6853 showing [O III] emission (green), $H\alpha$ (red), and broadband emission from Bessel B at 429 nm (blue): European Southern Observatory image eso9846a. North and east are indicated in the figure. The smallest ($22''$) and largest ($69''$) beam sizes, corresponding to the CO: $J = 3 \rightarrow 2$ and HCO^+ : $J = 1 \rightarrow 0$ transitions, are overlaid on the figure at the observed position, in red and blue. (b) Spectra of CO, HCO^+ , and CS observed toward that position in NGC 6853. The $J = 3 \rightarrow 2$, and $J = 2 \rightarrow 1$ transitions of CO, the $J = 3 \rightarrow 2$ transition of HCO^+ , and the $J = 5 \rightarrow 4$ transition of CS were measured with the ARO SMT (resolution 1 MHz, smoothed to 2 MHz; temperature scale is T_A^*). The $J = 1 \rightarrow 0$ transitions of CO and HCO^+ , and the $J = 3 \rightarrow 2$ and $J = 2 \rightarrow 1$ transitions of CS were measured using the ARO 12 m (resolution 1 MHz; temperature scale is T_R^*). Galactic contamination is present near 15 km s^{-1} in the $J = 2 \rightarrow 1$ and $J = 1 \rightarrow 0$ transitions of CO. A full spectrum is inset in the upper left corner of the CO: $J = 1 \rightarrow 0$ panel. Red and blueshifted velocity components are present in the spectra, sampling smaller-scale velocity structure of the $5'$ sized nebula.

(A color version of this figure is available in the online journal.)

because the nebula is thought to have a bipolar morphology, perhaps best represented as a clumpy cylinder or “barrel” with red and blueshifted halves tilted with respect to the line of sight (e.g., Bachiller et al. 1989; Kwok et al. 2008; O’Dell et al. 2013; Zeigler et al. 2013). The Ring thus resembles the Helix Nebula, except it is younger and less extended (~ 1.5 and opposed to $15'$). The varying beam sizes used in these observations sample different regions of the “barrel.” The larger beams ($\sim 60''$) encompass the bulk of the barrel, and consequently the whole range of gas velocities, while the smaller beams couple primarily

with the blue and redshifted rims (see Zeigler et al. 2013). As is evident in the CO: $J = 2 \rightarrow 1$ image of the Ring (Bachiller et al. 1989), the molecular gas extends well beyond the [N II] and vibrationally excited H_2 emission (Speck et al. 2003), and fills most of the apparent void in the center of the nebula traced in He II. To account for the complicated velocity structure, the data were fit with two to four velocity components, depending on the line profile (see Table 3). Additional velocity spatial information is clearly needed for the Ring to fully assess the geometric distribution of the molecular gas.

Table 3
Line Parameters for Observed Molecules^a

Source	Molecule	Transition	Velocity Component	V_{LSR} (km s^{-1})	T_A^* or T_R^* (K)	$\Delta V_{1/2}$ (km s^{-1})	$\int T_A^* dV$ or $\int T_R^* dV$ (K km s^{-1})	Notes	
K4-47	CO	$J = 6 \rightarrow 5$	Central	-23.4 ± 0.8	0.041 ± 0.017	22.6 ± 0.8	0.94 ± 0.01		
			Plateau	~ -25	0.020 ± 0.017	~ 60	~ 0.89		
		$J = 3 \rightarrow 2$	Central	-26.5 ± 0.3	0.140 ± 0.012	23.0 ± 0.7	3.43 ± 0.09		
			Plateau	~ -25	0.020 ± 0.012	~ 60	~ 0.89		
	HCO ⁺	$J = 2 \rightarrow 1$	Central	-26.2 ± 0.3	0.179 ± 0.004	19.6 ± 0.7	3.75 ± 0.12		
			Central	-25.8 ± 0.7	0.049 ± 0.007	19.6 ± 1.5	0.97 ± 0.07		
		$J = 3 \rightarrow 2$	Central	-26.9 ± 1.1	0.012 ± 0.005	22.6 ± 1.1	0.30 ± 0.01		
			Plateau	~ -28	0.006 ± 0.003	~ 60	~ 0.27		
	CS	$J = 5 \rightarrow 4$	Central	-24.6 ± 1.2	0.004 ± 0.002	16.7 ± 2.8	0.09 ± 0.01		
			Plateau	-25.0 ± 2.4	0.002 ± 0.001	~ 60	~ 0.07		
		$J = 3 \rightarrow 2$	Central	-28.0 ± 1.2	0.002 ± 0.0007	22.3 ± 1.2	0.04 ± 0.01		
			Plateau	~ -22	0.001 ± 0.0007	~ 60	~ 0.04		
NGC 6537	CO	$J = 6 \rightarrow 5$	Central	-23.0 ± 1.3	0.003 ± 0.001	19.1 ± 2.7	0.05 ± 0.01		
			Central	-27.3 ± 3.5	0.001 ± 0.0005	19.8 ± 6.1	0.01 ± 0.01		
		$J = 4 \rightarrow 3$	Central	10.1 ± 0.1	0.753 ± 0.052	12.9 ± 0.3	10.32 ± 0.22	b	
			Central	9.9 ± 0.4	1.23 ± 0.13	12.5 ± 0.5	16.47 ± 0.60		
	HCO ⁺	$J = 3 \rightarrow 2$	Central	9.7 ± 0.4	0.958 ± 0.017	13.5 ± 1.1	13.80 ± 0.92	b, c	
			Central	8.4 ± 1.0	0.693 ± 0.006	13.4 ± 2.4	9.89 ± 1.55	b, c	
		$J = 2 \rightarrow 1$	Central	9.3 ± 0.1	0.128 ± 0.003	11.6 ± 0.2	1.58 ± 0.02	b, c	
			Central	8.8 ± 0.5	0.034 ± 0.005	10.7 ± 1.0	0.39 ± 0.04	b, c	
	CS	$J = 5 \rightarrow 4$	Central	10.1 ± 0.1	0.035 ± 0.002	10.1 ± 0.3	0.38 ± 0.01	b	
			Central	9.3 ± 0.3	0.044 ± 0.002	12.1 ± 0.6	0.56 ± 0.03	b, c	
		$J = 3 \rightarrow 2$	Central	9.9 ± 1.0	0.034 ± 0.005	12.3 ± 1.7	0.45 ± 0.07	b, c	
			Central	16.5 ± 1.2	0.059 ± 0.026	35.0 ± 2.3	2.20 ± 0.15		
M2-48	CO	$J = 6 \rightarrow 5$	Central	16.6 ± 1.2	0.173 ± 0.064	36.0 ± 2.7	6.64 ± 0.45		
			Central	~ 16	~ 0.18	~ 35	~ 6.8	d	
		$J = 3 \rightarrow 2$	Central	~ 16	~ 0.1	~ 35	~ 3.7	d	
			Central	18.1 ± 0.7	0.028 ± 0.004	36.7 ± 1.5	1.10 ± 0.04		
	HCO ⁺	$J = 3 \rightarrow 2$	Central	15.2 ± 1.3	0.016 ± 0.002	38.8 ± 2.6	0.66 ± 0.04		
			Central	18.1 ± 2.1	0.002 ± 0.001	33.7 ± 3.6	0.06 ± 0.01		
		$J = 1 \rightarrow 0$	Central	15.0 ± 3.0	0.002 ± 0.0007	32.9 ± 5.7	0.08 ± 0.01	e	
			Central	18.4 ± 3.0	0.001 ± 0.0005	34.0 ± 6.0	0.05 ± 0.01		
	NGC 6720	CO	$J = 3 \rightarrow 2$	Red	15.1 ± 0.3	0.202 ± 0.020	6.1 ± 0.6	1.32 ± 0.20	
				Central	2.1 ± 0.8	0.094 ± 0.020	18.0 ± 2.1	1.79 ± 0.19	
				Blue	-19.5 ± 0.6	0.088 ± 0.020	10.5 ± 1.4	0.98 ± 0.11	
				Secondary blue	-33.2 ± 1.9	0.026 ± 0.020	10.0 ± 2.4	0.28 ± 0.09	
$J = 2 \rightarrow 1$			Red	15.7 ± 2.6	0.167 ± 0.004	7.0 ± 2.6	1.25 ± 0.08	e	
			Central	2.1 ± 2.6	0.023 ± 0.004	13.5 ± 2.6	0.34 ± 0.07	e	
			Blue	-16.4 ± 2.6	0.071 ± 0.004	12.8 ± 2.6	0.97 ± 0.07	e	
			Secondary blue	-36.8 ± 2.6	0.014 ± 0.004	13.5 ± 2.6	0.20 ± 0.07	e	
$J = 1 \rightarrow 0$			Red	12.7 ± 2.6	0.057 ± 0.005	9.5 ± 2.6	0.58 ± 0.04		
			Central	-0.3 ± 2.6	0.047 ± 0.005	14.1 ± 2.6	0.70 ± 0.04		
			Blue	-19.4 ± 2.6	0.030 ± 0.005	12.5 ± 2.6	0.39 ± 0.04		
			Blue	14.6 ± 0.4	0.010 ± 0.002	8.3 ± 0.9	0.09 ± 0.01	e	
HCO ⁺	$J = 3 \rightarrow 2$	Blue	-17.7 ± 1.2	0.004 ± 0.002	15.8 ± 2.1	0.07 ± 0.01	e		
		Blue	11.8 ± 3.4	0.020 ± 0.002	11.6 ± 3.4	0.24 ± 0.03			
	$J = 1 \rightarrow 0$	Central	0.1 ± 3.4	0.019 ± 0.002	12.9 ± 3.4	0.26 ± 0.03			
		Blue	-13.4 ± 3.4	0.016 ± 0.002	15.8 ± 3.4	0.26 ± 0.03			
CS	$J = 5 \rightarrow 4$	Red	16.2 ± 0.3	0.006 ± 0.001	6.1 ± 0.7	0.04 ± 0.01			
		Central	0.5 ± 1.9	0.0015 ± 0.001	11.7 ± 4.8	0.02 ± 0.01			
		Blue	-18.1 ± 1.2	0.002 ± 0.001	12.1 ± 2.7	0.03 ± 0.01			
		Blue	-18.1 ± 1.2	0.002 ± 0.001	12.1 ± 2.7	0.03 ± 0.01			
	$J = 3 \rightarrow 2$	Red	15.4 ± 0.4	0.010 ± 0.001	6.7 ± 1.0	0.07 ± 0.01			
		Central	1.3 ± 1.8	0.003 ± 0.001	6.7 ± 4.0	0.02 ± 0.01			
		Blue	-16.1 ± 1.6	0.004 ± 0.001	14.9 ± 2.9	0.07 ± 0.01			
		Blue	14.4 ± 0.8	0.005 ± 0.001	7.8 ± 1.9	0.04 ± 0.01			
$J = 2 \rightarrow 1$	Red	~ 2	0.002 ± 0.001	~ 12	~ 0.03	f			
	Central	~ 2	0.002 ± 0.001	~ 12	~ 0.03	f			
	Blue	~ -16	0.003 ± 0.001	~ 16	~ 0.05				
	Blue	~ -16	0.003 ± 0.001	~ 16	~ 0.05				
NGC 6853	CO	$J = 3 \rightarrow 2$	Red	-4.3 ± 0.4	0.072 ± 0.016	8.8 ± 1.0	0.68 ± 0.06		
			Blue	-34.9 ± 0.2	0.157 ± 0.016	8.0 ± 0.4	1.34 ± 0.06		
	$J = 2 \rightarrow 1$	Red	-5.2 ± 0.2	0.070 ± 0.004	7.4 ± 0.6	0.56 ± 0.03	c		
		Blue	-36.8 ± 0.1	0.181 ± 0.004	10.0 ± 0.2	1.93 ± 0.03	c		
	$J = 1 \rightarrow 0$	Red	-4.0 ± 2.8	0.030 ± 0.006	8.7 ± 4.9	0.28 ± 0.13	c		
		Blue	-36.4 ± 1.0	0.067 ± 0.006	13.1 ± 2.8	0.93 ± 0.16	c		

Table 3
(Continued)

Source	Molecule	Transition	Velocity Component	V_{LSR} (km s ⁻¹)	T_A^* or T_R^* (K)	$\Delta V_{1/2}$ (km s ⁻¹)	$\int T_A^* dV$ or $\int T_R^* dV$ (K km s ⁻¹)	Notes
	HCO ⁺	$J = 3 \rightarrow 2$	Red	-4.0 ± 1.0	0.005 ± 0.002	9.4 ± 2.7	0.05 ± 0.01	e
			Blue	-36.6 ± 0.5	0.010 ± 0.002	11.6 ± 1.6	0.13 ± 0.01	e
	CS	$J = 1 \rightarrow 0$	Red	0.7 ± 1.8	0.005 ± 0.001	23.8 ± 4.3	0.12 ± 0.02	
			Blue	-36.2 ± 0.3	0.021 ± 0.001	10.9 ± 0.6	0.21 ± 0.01	
			Red	-6.5 ± 0.5	0.003 ± 0.0005	7.3 ± 1.5	0.02 ± 0.01	e
			Blue	-31.1 ± 1.7	0.001 ± 0.0005	14.6 ± 4.2	0.03 ± 0.01	e
	CS	$J = 3 \rightarrow 2$	Red	-7.3 ± 0.4	0.006 ± 0.001	4.4 ± 0.9	0.03 ± 0.01	
			Blue	-32.8 ± 1.7	0.003 ± 0.001	12.2 ± 4.1	0.08 ± 0.01	
			Red	-3.2 ± 0.6	0.005 ± 0.0007	8.9 ± 1.5	0.05 ± 0.01	
			Blue	-39.1 ± 2.5	0.002 ± 0.0007	12.2 ± 7.6	0.06 ± 0.02	

Notes.

^a Measured with 1 MHz resolution unless otherwise noted; T_A^* and T_R^* apply to SMT and 12 m data, respectively (See Table 2); uncertainties are $\pm 1.5\sigma$.

^b From Edwards & Ziurys (2013).

^c Galactic contamination on redshifted edge of line; see Figures 2(b) and 5(b).

^d Galactic contamination blended with line profile; see Figure 3(b).

^e Measured with 2 MHz resolution.

^f Blended components; see Figure 4(b).

3.6. NGC 6853 (Dumbbell Nebula)

4. ANALYSIS

The Dumbbell Nebula (NGC 6853) is the oldest PN in this sample with an age of $10,000_{-1,300}^{+1,900}$ yr (O’Dell et al. 2002). The uncertainty of this value is small because the object is relatively close such that its distance is better known. The object hosts emission from numerous atomic lines, including H α , He I, He II, [N II], [O III], and [Ne III] (e.g., Hua & Louise 1970; Hawley & Miller 1978; Papamastorakis et al. 1993). The classic “dumbbell” shape is readily visible in lower excitation lines of [O I] and [N II], while more energetic transitions such as He II sample the central region (e.g., Meaburn et al. 2005). NGC 6853 exhibits intense vibrationally excited H₂ lines, observed both in the infrared and in the UV (Zuckerman & Gatley 1988; Kastner et al. 1996; Lupu et al. 2006; Kwok et al. 2008). The dumbbell structure is apparent in the H₂, as well (Kwok et al. 2008), which may exist in dense clumps, similar to the Helix Nebula (Meaburn & López 1993). The first CO detection in the Dumbbell was by Huggins et al. (1996), who observed the $J = 2 \rightarrow 1$ transition toward this object. A combined infrared and millimeter study using the *Infrared Space Observatory* and the IRAM 30 m was subsequently carried out by Bachiller et al. (2000). These authors mapped the $J = 2 \rightarrow 1$ and $J = 1 \rightarrow 0$ transitions of CO across a roughly $4' \times 5'$ region; at various positions, the spectra exhibited multiple velocity components indicative of a clumpy and filamentary structure, although the dumbbell shape was not obvious in CO.

The offset position ($\Delta\alpha = -68''$, $\Delta\delta = -63''$) was observed in this study, located near the southwestern lobe of the Dumbbell (Figure 5(a)), and chosen based on the previous CO work. As shown in Figure 5(b), the spectra here are double-peaked, with clearly defined blueshifted and redshifted components near approximately -35 km s⁻¹ and -5 km s⁻¹, respectively, similar to what was observed by Huggins et al. (1996). The linewidths of both components are typically 8–12 km s⁻¹. The relative intensities of the two components appear to vary between molecules, with the blueshifted one more intense for CO and HCO⁺, and the redshifted for CS. This effect cannot be explained by differences in beam sizes. The line profiles imply that there are obvious chemical and kinematic complexities in this source.

In order to establish molecular abundances, two methods were employed. For CO and CS, where at least three transitions were observed, rotational diagrams were created for each source (Turner 1991). Here the level populations are assumed to be governed by a single rotational temperature, T_{rot} , under the LTE approximation. Uncertainties in this analysis are based on the goodness of the fit. The data were also modeled using a non-LTE, statistical equilibrium radiative transfer code, RADEX (van der Tak et al. 2007). This code balances collisional excitation with radiative decay using the escape probability formalism, assuming an isothermal, homogeneous medium. Gas kinetic temperatures T_K , densities $n(\text{H}_2)$, and molecular column densities N_{tot} are determined by matching the model predictions to the observed spectral-line brightness temperatures. For CO and CS, all three variables could be independently determined from RADEX because three rotational transitions were measured. For HCO⁺, on the other hand, only two transitions were observed. In this case, the kinetic temperature T_K was held fixed to that determined for CS, which has a dipole moment closer in value to HCO⁺ than CO, while the H₂ density and column density were varied. Modeling was conducted over temperature and density ranges of 5–200 K and 10^4 – 10^7 cm⁻³. For the extended Ring and Dumbbell Nebulae, a uniform filling factor was assumed in the analyses. For the other three sources, a beam filling factor correction was applied to the main beam brightness temperatures T_R . The filling factor was based on source sizes derived from the optical images, given in Table 1. The modeling results are given in Table 4. Uncertainties for the RADEX fits were based on those in the measured antenna temperature and line width, as given in Table 2. Note that for all sources, column densities determined by RADEX are in excellent agreement with those from the rotational diagram, lending credence to the derived parameters.

In order to estimate fractional abundances, H₂ column densities had to be established for each source. All objects except M2-48 had been observed in 2.12 μm H₂ emission (Kastner et al. 1996; Davis et al. 2003; Speck et al. 2003; S. Baldrige et al. in preparation). The H₂ column density was therefore calculated from the beam-averaged surface brightness from these

Table 4
Measured Abundances in Observed Planetary Nebulae

Source	Component	Molecule	Rotational Diagram		Radiative Transfer Modeling			$f(X)^a$
			T_{rot} (K)	N (cm^{-2})	T_{K} (K)	$n(\text{H}_2)$ (cm^{-3})	N_{tot} (cm^{-2})	
K4-47	Central	CO	10	$3.4 \pm 0.3 \times 10^{16}$	10	2.0×10^5	$5.1 \pm 0.9 \times 10^{16}$	$1.8 \pm 0.3 \times 10^{-4}$
		CS	11	$5.1 \pm 0.3 \times 10^{12}$	39	4.5×10^5	$5.4 \pm 3.6 \times 10^{12}$	$1.9 \pm 1.3 \times 10^{-8}$
		HCO ⁺			39 ^b	1.8×10^5	$4.4 \pm 1.5 \times 10^{12}$	$1.5 \pm 0.5 \times 10^{-8}$
NGC 6537		CO	49	$9.4 \pm 0.1 \times 10^{15}$	62	2.0×10^5	$1.0 \pm 0.1 \times 10^{16}$	$4.3 \pm 0.5 \times 10^{-5}$
		CS	9	$1.0 \pm 0.2 \times 10^{13}$	76	1.0×10^5	$9.9 \pm 1.1 \times 10^{12}$	$4.3 \pm 0.5 \times 10^{-8}$
		HCO ⁺			76 ^b	1.5×10^5	$2.2 \pm 0.3 \times 10^{12}$	$9.6 \pm 1.1 \times 10^{-9}$
M2-48		CO			45	1.3×10^5	$4.5 \pm 1.8 \times 10^{15}$	10^{-4c}
		CS	10	$1.0 \pm 0.5 \times 10^{12}$	55	1.4×10^5	$1.2 \pm 0.7 \times 10^{12}$	$2.7 \pm 1.5 \times 10^{-8}$
		HCO ⁺			55 ^b	6.2×10^4	$5.0 \pm 0.9 \times 10^{12}$	$1.1 \pm 0.2 \times 10^{-7}$
NGC 6720	Red	CO	37	$1.0 \pm 0.3 \times 10^{15}$	38	2.0×10^5	$1.0 \pm 0.5 \times 10^{15}$	$3.7 \pm 1.7 \times 10^{-5}$
		CS	15	$2.5 \pm 0.6 \times 10^{11}$	45	9.0×10^5	$2.5 \pm 1.0 \times 10^{11}$	$9.3 \pm 3.7 \times 10^{-9}$
		HCO ⁺			45 ^b	1.8×10^5	$1.5 \pm 0.6 \times 10^{11}$	$5.6 \pm 2.1 \times 10^{-9}$
	Blue	CO	29	$6.7 \pm 0.7 \times 10^{14}$	37	3.0×10^5	$7.5 \pm 2.9 \times 10^{14}$	$2.8 \pm 1.1 \times 10^{-5}$
		CS	13	$2.6 \pm 0.2 \times 10^{11}$	44	5.9×10^5	$2.6 \pm 1.6 \times 10^{11}$	$9.6 \pm 6.0 \times 10^{-9}$
		HCO ⁺			44 ^b	8.6×10^4	$2.3 \pm 1.2 \times 10^{11}$	$8.5 \pm 4.4 \times 10^{-9}$
NGC 6853	Red	CO	23	$4.7 \pm 0.5 \times 10^{14}$	27	2.1×10^5	$4.3 \pm 2.5 \times 10^{14}$	$1.5 \pm 0.9 \times 10^{-5}$
		CS	12	$2.2 \pm 0.1 \times 10^{11}$	36	7.0×10^5	$2.2 \pm 0.9 \times 10^{11}$	$7.6 \pm 3.0 \times 10^{-9}$
		HCO ⁺			36 ^b	4.3×10^5	$5.2 \pm 2.6 \times 10^{10}$	$1.8 \pm 0.9 \times 10^{-9}$
	Blue	CO	22	$1.2 \pm 0.2 \times 10^{15}$	22	3.2×10^5	$1.3 \pm 0.5 \times 10^{15}$	$4.5 \pm 1.8 \times 10^{-5}$
		CS	11	$1.4 \pm 0.3 \times 10^{11}$	32	6.0×10^5	$1.4 \pm 0.6 \times 10^{11}$	$4.8 \pm 2.2 \times 10^{-9}$
		HCO ⁺			32 ^b	2.2×10^5	$2.2 \pm 0.6 \times 10^{11}$	$7.6 \pm 1.9 \times 10^{-9}$

Notes.^a Relative to H₂.^b Fixed to value from CS fit.^c Assumed value.

measurements, using the relationship of O’Dell et al. (2005), scaled by the appropriate excitation temperature. For the older nebulae, 900 K was assumed, modeled on that estimated for the Helix (Cox et al. 1998); the younger PNe (K4-47 and NGC 6537) appear to be warmer, and in these cases $T_{\text{ex}} \sim 1550$ K and 1200 K were used, based on Lumsden et al. (2001). There are currently no H₂ measurements for M2-48, and as a consequence, the column density of this molecule was scaled from that measured for CO, assuming CO/H₂ $\sim 10^{-4}$, as determined for the Helix Nebula (Zack & Ziurys 2013). The H₂ column densities so derived are given in Table 1, and the resulting fractional abundances in Table 4.

For K4-47, only the main (“central”) velocity component was modeled, because there was limited data for the secondary “plateau” feature. The rotational diagram analysis yielded rotational temperatures of $T_{\text{rot}} = 10$ K and 11 K for CO and CS, respectively. From the RADEX modeling of CO, the kinetic temperature was found to be $T_{\text{K}} \approx 10$ K with a density of $n(\text{H}_2) \approx 2.0 \times 10^5 \text{ cm}^{-3}$, while the CS analysis suggests $T_{\text{K}} \approx 39$ K, and $n(\text{H}_2) \approx 4.5 \times 10^5 \text{ cm}^{-3}$. The kinetic temperatures are consistent with the rotational diagrams. Because CO has a low dipole moment of $\mu_0 = 0.11$ D (Pickett et al. 1998), it is expected that $T_{\text{rot}} \approx T_{\text{K}}$. For CS, the dipole moment is larger ($\mu_0 = 1.96$ D), such that $T_{\text{rot}} < T_{\text{K}}$. Almost identical column densities were obtained for CO and CS from the two methods: $N_{\text{tot}}(\text{CO}) \sim 3\text{--}5 \times 10^{16} \text{ cm}^{-2}$ and $N_{\text{tot}}(\text{CS}) \sim 5 \times 10^{12} \text{ cm}^{-2}$ (see Table 4). The analysis for HCO⁺ resulted in $n(\text{H}_2) \approx 1.8 \times 10^5 \text{ cm}^{-3}$ and $N_{\text{tot}} \approx 4.4 \times 10^{12} \text{ cm}^{-2}$. Using the derived H₂ column density of $N_{\text{tot}} \approx 2.9 \times 10^{20} \text{ cm}^{-2}$, the fractional abundances for CO, CS, and HCO⁺ are $f \sim 1.8 \times 10^{-4}$, $f \sim 1.9 \times 10^{-8}$, and $f \sim 1.5 \times 10^{-8}$, respectively.

The modeling results for NGC 6537 were previously reported by Edwards & Ziurys (2013), except for a few minor differences. For CO, the $J = 4 \rightarrow 3$ line was added to the previous analysis, but without significant change to either the rotational diagram or the RADEX results ($T_{\text{rot}} \approx 50$ K, $T_{\text{K}} \approx 62$ K, $n(\text{H}_2) \approx 2 \times 10^5 \text{ cm}^{-3}$, and $N_{\text{tot}} \approx 1.0 \times 10^{16} \text{ cm}^{-2}$). In the case of HCO⁺, the kinetic temperature chosen here for the RADEX modeling was $T_{\text{K}} = 76$ K, that derived from CS, instead of 62 K used previously (see Edwards & Ziurys 2013). As a consequence, the gas density and HCO⁺ column density decreased slightly from the earlier values to $n(\text{H}_2) \approx 1.5 \times 10^5 \text{ cm}^{-3}$ and $N_{\text{tot}} \approx 2.2 \times 10^{12} \text{ cm}^{-2}$. The CS results did not change ($T_{\text{rot}} \approx 9$ K, $T_{\text{K}} \approx 76$ K, $n(\text{H}_2) \approx 10^5 \text{ cm}^{-3}$, and $N_{\text{tot}} \approx 1 \times 10^{13} \text{ cm}^{-2}$). In addition, a somewhat higher excitation temperature was used here in deriving the H₂ column density than that of Edwards & Ziurys (1200 K versus 900 K), increasing it by a factor of ~ 2.5 . The revised abundances for CO, CS, and HCO⁺ are $f \sim 4.3 \times 10^{-5}$, $f \sim 4.3 \times 10^{-8}$, and $f \sim 9.6 \times 10^{-9}$.

Because of significant Galactic contamination in the $J = 2 \rightarrow 1$ and $J = 3 \rightarrow 2$ transitions of CO in M2-48 (Figure 3(b)), a rotational diagram analysis was only performed for CS for this source, for which $T_{\text{rot}} \approx 10$ K and $N_{\text{tot}} = 1.0 \times 10^{12} \text{ cm}^{-2}$ was found. The radiative transfer analysis for CS yielded $T_{\text{K}} \approx 55$ K, $n(\text{H}_2) \approx 1.4 \times 10^5 \text{ cm}^{-3}$, and $N_{\text{tot}} \approx 1.2 \times 10^{12} \text{ cm}^{-2}$, in excellent agreement. For CO, the RADEX fits gave $T_{\text{K}} \approx 45$ K, $n(\text{H}_2) \approx 1.3 \times 10^5 \text{ cm}^{-3}$, and $N_{\text{tot}} \approx 4.5 \times 10^{15} \text{ cm}^{-2}$, using a rough estimate of the $J = 3 \rightarrow 2$ intensity. The analysis for HCO⁺ produced $n(\text{H}_2) \approx 6.2 \times 10^4 \text{ cm}^{-3}$, and $N_{\text{tot}} \approx 5.0 \times 10^{12} \text{ cm}^{-2}$. The calculated abundances of CS, and HCO⁺ are $f \sim 2.7 \times 10^{-8}$, and $f \sim 1.7 \times 10^{-7}$, assuming a CO/H₂ $\sim 10^{-4}$ for lack of H₂ measurements, as mentioned.

For the Ring Nebula, only the red and blueshifted velocity components were modeled, as they were consistently present in all observed transitions. The rotational diagram analysis yielded $T_{\text{rot}} \approx 37$ K and 29 K for the red and blueshifted components of CO, and 15 K and 13 K for the corresponding features in CS. RADEX modeling of both components yielded $T_{\text{K}} \sim 37\text{--}38$ K, and $n(\text{H}_2) \sim 2\text{--}3 \times 10^5 \text{ cm}^{-3}$ for CO, and $T_{\text{K}} \sim 44\text{--}45$ K, and $n(\text{H}_2) \sim 6\text{--}9 \times 10^5 \text{ cm}^{-3}$ for CS—very consistent with the rotational diagram temperatures. Both methods yielded very similar column densities of $N_{\text{tot}} \sim 1 \times 10^{15} \text{ cm}^{-2}$ and $N_{\text{tot}} \sim 7 \times 10^{14} \text{ cm}^{-2}$ for the red and blueshifted CO, respectively, as also found for CS with $N_{\text{tot}} \approx 2.5 \times 10^{11} \text{ cm}^{-2}$ (red) and $N_{\text{tot}} \approx 2.6 \times 10^{11} \text{ cm}^{-2}$ (blue). In the case of HCO^+ , $n(\text{H}_2) \sim 1.8 \times 10^5 \text{ cm}^{-3}$ (red) and $9 \times 10^4 \text{ cm}^{-3}$ (blue), with $N_{\text{tot}} \sim 1.5\text{--}2.3 \times 10^{11} \text{ cm}^{-2}$ (see Table 4). Abundances for both velocity components are very similar in all three molecules, falling in the ranges $f(\text{CO}) \sim 2.8\text{--}3.7 \times 10^{-5}$, $f(\text{CS}) \sim 9.3\text{--}9.6 \times 10^{-9}$, and $f(\text{HCO}^+) \sim 5.6\text{--}8.5 \times 10^{-9}$.

Both red and blueshifted components were also analyzed separately for the one position observed in the Dumbbell Nebula. For CO, results for both features were very similar, with $T_{\text{rot}} \sim 22\text{--}23$ K, $T_{\text{K}} \sim 22\text{--}27$ K, and $n(\text{H}_2) \sim 2\text{--}3 \times 10^5 \text{ cm}^{-3}$. The column densities slightly varied, with $N_{\text{tot}} \sim 4.3\text{--}4.7 \times 10^{14} \text{ cm}^{-2}$ for the redshifted component and $N_{\text{tot}} \sim 1.2\text{--}1.3 \times 10^{15} \text{ cm}^{-2}$ for the blueshifted one, where the range reflects the two analysis methods. For CS, the red and blue components had virtually identical fits, $T_{\text{rot}} \approx 11\text{--}12$ K and $T_{\text{K}} \approx 32\text{--}36$ K, while $n(\text{H}_2) \sim 6\text{--}7 \times 10^5 \text{ cm}^{-3}$. Both methods yielded identical CS column densities of $N_{\text{tot}} \approx 2.2 \times 10^{11} \text{ cm}^{-2}$ (red) and $N_{\text{tot}} \approx 1.4 \times 10^{11} \text{ cm}^{-2}$ (blue). Fits to the red and blueshifted lines for HCO^+ yielded $n(\text{H}_2) \approx 4.3 \times 10^5 \text{ cm}^{-3}$ and $N_{\text{tot}} \approx 5.2 \times 10^{10} \text{ cm}^{-2}$ and $n(\text{H}_2) \approx 2.2 \times 10^5 \text{ cm}^{-3}$ and $N_{\text{tot}} \approx 2.2 \times 10^{11} \text{ cm}^{-2}$. Fractional abundances lie in the ranges $f \sim 1.5\text{--}4.5 \times 10^{-5}$, $f \sim 4.8\text{--}7.6 \times 10^{-9}$, and $f \sim 1.8\text{--}7.6 \times 10^{-9}$ for CO, CS, and HCO^+ , respectively.

5. DISCUSSION

5.1. Physical Conditions and Morphological Implications

The molecular material in the five PNe studied appears to arise from relatively warm and dense gas. Modeled kinetic temperatures ranged from 10–62 K (CO) and 32–76 K (CS), with densities of $n(\text{H}_2) \sim 0.1\text{--}1 \times 10^6 \text{ cm}^{-3}$, based on all three molecules. CS typically traces slightly warmer and denser gas than CO, which can be understood in terms of its higher dipole moment. Gas densities derived from HCO^+ are similar to those of CS. There appears to be a slight decrease in the kinetic temperatures as a function of age, with the exception of K4-47. K4-47 is the youngest source observed and, surprisingly, also the coldest, but this result may simply reflect beam dilution. The temperatures and density values established for these five sources are consistent with those found for other PNe. For the Helix, the oldest known PN, Zack & Ziurys (2013) found $T_{\text{K}} \approx 10\text{--}40$ K, and $n(\text{H}_2) \approx 0.1\text{--}5 \times 10^5 \text{ cm}^{-3}$, based on CO and H_2CO measurements. Observations of the young PN NGC 7027 suggest densities from $1\text{--}5 \times 10^5 \text{ cm}^{-3}$ and $T_{\text{ex}} \sim 35\text{--}40$ K (Zhang et al. 2008; Hasegawa & Kwok 2001). Bachiller et al. (1997) estimated similar values of $T_{\text{K}} \sim 25\text{--}60$ K and $n(\text{H}_2) \sim 1\text{--}4 \times 10^5 \text{ cm}^{-3}$ for a sample of PPNe and PNe. The densities are also consistent with estimates from vibrationally excited H_2 emission, which indicate $n(\text{H}_2) \sim 10^6 \text{ cm}^{-3}$ (O’Dell et al. 2005). In general, molecules appear to be present in dense, self-shielding clumps in PNe.

The line profiles measured in these PNe offer some insight into their morphology. For K4-47, the broad plateau feature, prominent in the $J = 6 \rightarrow 5$ line of CO and the $J = 3 \rightarrow 2$ transition of HCO^+ , may be sampling the two high-velocity knots visible in $[\text{N II}]$, which exhibit broad line profiles of $75\text{--}90 \text{ km s}^{-1}$, indicative of shock acceleration (e.g., Corradi et al. 2000). The outflow associated with the knots is thought to be inclined $65^\circ\text{--}70^\circ$ with respect to the line of sight, suggesting velocities of $100\text{--}150 \text{ km s}^{-1}$. The line width at zero power in the CO line is roughly 90 km s^{-1} , consistent with the knot profiles. The presence of both CO and HCO^+ in the high-velocity material is consistent with the knots having Type I PN abundances, as proposed by Gonçalves et al. (2004).

NGC 6537 is possibly multi-polar in nebular shape (Cuesta et al. 1995). Although there are a few suggestive “shoulder”-like features (see Figure 2(b)), the line profiles from this source for the most part trace only one main central velocity component near 10 km s^{-1} . Even the $J = 1 \rightarrow 0$ line of HCO^+ shows little evidence of any asymmetry, although it was measured with the largest beam size of $69''$, which encompasses part of the quadrupolar optical structure (Figure 2(a)). Because the Red Spider is relatively young, perhaps the remnant molecular material has not been sufficiently accelerated in the polar outflows. M2-48 is also thought to be bipolar (López-Martin et al. 2002). The larger beam sizes in this study do include the collimated outflow in this source (see Figure 3(a)), although not the bow-shocked rims, which lie further out. There is certainly some hint of red and blueshifted asymmetry in the $J = 2 \rightarrow 1$ transition of CO and the HCO^+ $J = 1 \rightarrow 0$ line. Again, the molecular gas does not appear to be a good tracer of the bipolar structure in this nebula.

The two other nebulae studied, also the oldest, exhibit spectra with distinct red and blueshifted velocity components. In the case of the Ring, these components, near $V_{\text{LSR}} \sim +15$ and -18 km s^{-1} , are prominent in all transitions except the $J = 1 \rightarrow 0$ line of HCO^+ . Here the larger beam is likely tracing more material flowing perpendicular to the line of sight. The line profiles thus suggest that the bulk of the molecular material is almost directly flowing toward or away from the line of sight, i.e., a bipolar structure viewed approximately along the axis of the outflow, consistent with previous geometrical interpretations (e.g., Bachiller et al. 1989; Kwok et al. 2008; O’Dell et al. 2013). The Ring is therefore similar in structure to the “barrel” or cylindrical shape of the Helix Nebula (Zeigler et al. 2013), except it is somewhat younger and the hollow of the barrel is not as prominent. NGC 6853 is also a bipolar nebula with an axis slightly tilted ($\sim 15^\circ$) with respect to the plane of the sky, with a possible triple conic structure (Kwok et al. 2008). However, this nebula is quite extended ($>5'$) with respect to even the largest telescope beam used (see Figure 5(a)). The position chosen here is near the edge of southwest lobe. The red and blueshifted features in the spectra trace the complex velocity structure within that lobe, rather than the overall bipolar geometry. J. L. Edwards & L. M. Ziurys (2014, in preparation) have subsequently mapped the Dumbbell in HCO^+ emission, giving a global view of its molecular morphology.

5.2. Molecular Abundances Across 10,000 yr

As shown in Table 4, the abundances of CO, CS, and HCO^+ do not vary significantly between the five PNe. The total CO abundances, considering all velocity components for a given source, fall in the range $f \sim 0.4\text{--}1.8 \times 10^{-4}$ for all five nebulae, a difference of less than a factor of five. K4-47 has the highest

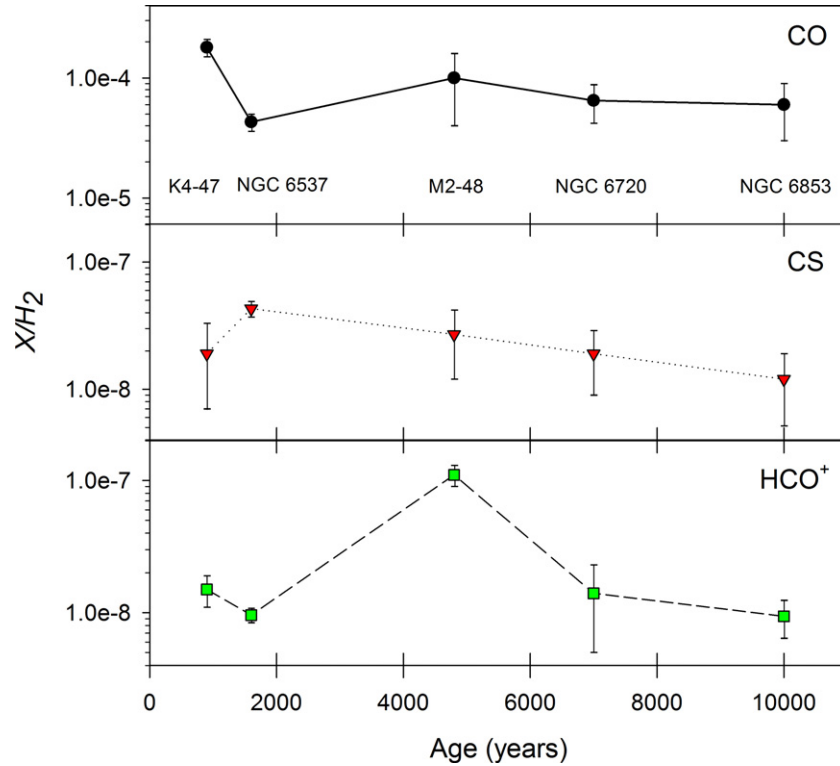


Figure 6. Plots of the molecular fractional abundances, relative to H_2 , measured in this study (log scale) as a function of nebular age. (Circles and solid lines: CO; triangles and dotted lines: CS; squares and dashed lines: HCO^+) Uncertainties in the abundances are given as error bars on the graphs. From this figure, it is clear that the molecular abundances from this sample do not significantly vary with age across a duration of $\sim 10,000$ yr.

(A color version of this figure is available in the online journal.)

fractional abundance of CO, and NGC 6537 (Red Spider) the lowest. For CS, the variation is even less, with $f \sim 1\text{--}4 \times 10^{-8}$. CS is most abundant in the Red Spider, and least prevalent in the Dumbbell. The fractional abundance of HCO^+ is $f \sim 10^{-8}$ for all five objects except M2-48, where $f \sim 10^{-7}$ —an order of magnitude higher. These values are similar to what has been measured at multiple positions in the Helix Nebula, where $f(CO/H_2) \sim 0.3\text{--}6 \times 10^{-4}$ and $f(HCO^+/H_2) \sim 0.3\text{--}7.3 \times 10^{-8}$ (Zack & Ziurys 2013). The average fractional abundance of HCO^+ across the entire Helix Nebula is $f \sim 10^{-8}$ (Zeigler et al. 2013).

Figure 6 shows the fractional abundances of all three molecules as a function of nebula age. As the figure shows, there are only minor variations between the five sources, and no apparent decreasing trend with age. The uncertainties in the age estimates (see Table 1) do not affect this conclusion. These observations contradict the predictions of chemical models of PNe (Redman et al. 2003). For example, Redman et al. calculate that the abundance of CO decreases by about an order of magnitude from ages 2550 yr ($f \sim 10^{-3}$) to 10,500 yr ($f \sim 2 \times 10^{-4}$). The CO abundances measured here not only are relatively constant with age, but are somewhat smaller than the model results. The CS abundance is also predicted to diminish with nebular age by a factor of ~ 1000 , with an initial value of 10^{-5} , decreasing to $\sim 2 \times 10^{-8}$. The measurements here suggest invariance as a function of age. The model, however, predicts a rather high CS abundance of 10^{-5} at 2550 yr, as compared to values of $10^{-7}\text{--}10^{-6}$ found in PPNe and many AGB stars (Kasuga et al. 1997; Zhang et al. 2009; Ziurys et al. 2009, and references therein). At 10,500 yr, however, Redman’s predicted abundance matches the observations for all sources, regardless of age. HCO^+ has largest discrepancy. Redman et al. compute

an abundance value of $\sim 10^{-10}$ at 2550 yr and $\sim 6 \times 10^{-12}$ at 10,500 yr. It is clear from these observations and that of the Helix Nebula (Zack & Ziurys 2013; Zeigler et al. 2013) that the abundances of HCO^+ in PNe are not less than 10^{-8} . Ali et al. (2001) predict $f(HCO^+/H_2) \sim 5 \times 10^{-9}$ for older nebulae (> 8000 yr), in better agreement. A more recent photoionization model for PNe by Kimura et al. (2012) underestimates the abundance of CS with respect to H_2 by at least a factor of 100, but reproduces the observed HCO^+ abundances fairly accurately. This code does not consider time evolution, but rather abundances as a function of ionization zone.

5.3. CS: A Common Species in Planetary Nebulae

CS was identified in all five PNe studied—a significant increase in the number of detections of this molecule. As mentioned, only one line of CS had previously been observed in PNe (Woods & Nyman 2005). Bachiller et al. (1997) had previously searched for the $J = 2 \rightarrow 1$ this molecule toward the Ring Nebula, among others, obtaining 3σ upper limits of ~ 20 mK in this object—consistent with the observed brightness temperature of ~ 4 mK. CS was also not detected in the young, C-rich PN NGC 7027 with a limit of ~ 8 mK (Zhang et al. 2008; Hasegawa & Kwok 2001). Bachiller et al. (1997) proposed that the absence of CS resulted from UV photodestruction, as it is a common molecule in both AGB envelopes and PPNe (see Ziurys et al. 2009). The observations conducted here demonstrate that the species still survives in the PN phase. Note that the CS emission lines are rather weak in the five source studied here, with $T_R \sim 10$ mK, except for NGC 6537, where they are ~ 30 mK.

The fractional abundances of CS with respect to H_2 in the C-rich PPNe CRL 2688 and CRL 618 are $f \sim 2\text{--}9 \times 10^{-7}$ (Kasuga et al. 1997; Bachiller et al. 1997). In carbon-rich AGB envelopes, it is about an order of magnitude higher at $f \sim 1\text{--}2 \times 10^{-6}$, while in O-rich shells $f \sim 10^{-7}\text{--}10^{-6}$ (Zhang et al. 2009; Ziurys et al. 2009, and references therein). The abundance of CS therefore is lower in PNe ($f \sim 1\text{--}4 \times 10^{-8}$) than in AGB stars and PPNe, suggesting some photodestruction in the early PN phase.

Systematically low sulfur abundances have been exhibited by PNe, when compared with H II regions of the same metallicity (Henry et al. 2004). There were a number of suggested explanations for these deficiencies, but Henry et al. (2012) conclude that the most likely reason is the sequestering of atomic sulfur into dust and/or molecules. The C/O ratio is critical in determining the chemical composition of dust and molecules that form in a circumstellar envelope (e.g., Tenenbaum et al. 2010), which will in turn influence the nature of the surviving material in PNe. In O-rich environments, it is postulated that any sulfide grains (MgS, CaS, FeS) that form will be oxidized, releasing the sulfur back into the gas phase (Henry et al. 2012). Sulfur is then available to create gas-phase molecules. However, in carbon-rich environments, such metal-sulfide grains remain in the solid state, removing sulfur from the gas-phase and producing elemental depletions.

All five nebulae studied here exhibit atomic sulfur emission. However, the deficiency of this element in K4-47 and M2-48 has not yet been examined; nor are their C/O ratios known. Both the Red Spider and the Dumbbell are not sulfur deficient. As shown in Table 1, they are also somewhat oxygen-rich and contain CS. In contrast, the C-rich PN NGC 7027 is slightly sulfur deficient, and does not have detectable CS emission. Our results are thus reasonably consistent with the Henry et al. (2012) hypothesis that O-rich environments contain gas-phase sulfur. The one possible exception is the Ring, which is somewhat oxygen-rich, has CS, but has a lack of atomic sulfur (Henry et al. 2004).

5.4. Major Influences in Nebular Chemistry

As a PN ages, the UV radiation field of the central proto-white dwarf steadily increases, bombarding the surrounding matter and creating a highly ionized environment. Molecules from the remnant AGB and PPN phases are thought to undergo severe photodissociation, leading to much reduced abundances over time, as discussed (e.g., Redman et al. 2003); photochemistry, however, is also predicted to be active (Ali et al. 2001; Kimura et al. 2012). For example, creation of C^+ leads to CO^+ , the major precursor to HCO^+ . The temperatures of the central stars are an indicator of the severity of the UV field in a given PN. As shown in Table 1, stellar temperatures are between 115,000–160,000 K for K4-47, NGC 6720, and NGC 6853; NGC 6537 has a much higher value of $\sim 340,000$ K, but the star in this object is one of the hottest known among PNe (Gonçalves et al. 2004; Matsuura et al. 2005; O’Dell et al. 2007; Rauch 2003). The stellar temperature for M2-48 is, unfortunately, not known. Such temperatures indicate strong UV radiation in these objects.

As discussed, this study demonstrates that these molecular abundances do not apparently decrease significantly with nebular age, starting near the onset of the PN phase. The abundance of CS does drop during the PPN stage, as noted, likely due to photodissociation. For HCO^+ , on the other hand, no significant decrease in abundance occurs from the AGB to the end of the PN

stage. The abundances found for HCO^+ in this sample, as well as in the Helix Nebula and NGC 7027 (Zack & Ziurys 2013; Zhang et al. 2008), are all very similar to what has been measured in the envelopes of O-rich stars, namely $f \sim 10^{-8}\text{--}10^{-7}$ (see Pulliam et al. 2011). This result is somewhat surprising, because NGC 7027 is quite carbon-rich, although the other nebulae have $O \geq C$. HCO^+ has only been detected on one C-rich AGB envelope, IRC+10216, with $f \sim 4 \times 10^{-9}$ —considerably less than that found in NGC 7027. Therefore, the chemistry in PNe can be accounted for by molecular survival from the AGB phase, coupled with nebular production and destruction, depending on the chemical species.

The progenitor mass must also influence the extent of the chemical complexity in PNe. The nebulae studied here all are thought to have evolved from more massive stars. A main sequence star with $M_* > 4 M_\odot$ was the origin of NGC 6537 (Pottasch et al. 2000; Matsuura et al. 2005). McCandliss et al. (2007) estimate the progenitor mass for the Dumbbell Nebula to be $\sim 3\text{--}4 M_\odot$. The main sequence mass estimate for NGC 7027 is also between $3\text{--}4 M_\odot$ (Bernard-Salas et al. 2001), and $\sim 6.5 M_\odot$ for the Helix (Henry et al. 1999). For the Ring Nebula, the progenitor star mass is more uncertain, but at least greater than $1 M_\odot$ (Sahai et al. 2012). These higher mass stars experience enhanced mass loss rates, which create more substantial shells and higher molecular circumstellar abundances. There is consequently more molecular material to be passed onto the PPN and PN phases. Huggins et al. (1996, 2005) have suggested that CO is detected only in PNe evolved from more massive ($> 2.4 M_\odot$) progenitors. Further molecular studies of PNe with low mass progenitor stars are clearly needed to examine this hypothesis.

5.5. Molecular Seeding of Diffuse Clouds

Recent observations by Liszt, Lucas, and collaborators (e.g., Liszt & Lucas 2001; Lucas & Liszt 2002; Liszt et al. 2006, 2008) have shown the presence of polyatomic molecules in diffuse clouds. This material remained undetected for some time, because the densities in such clouds are too low to allow for collisional excitation. Liszt et al. discovered these molecules by observing their low energy transitions in absorption against background quasars. The polyatomic species found by these authors by this method are HCO^+ , HCN, HNC, H_2CO , CCH, C_3H_2 , H_2S , NH_3 , and HCS^+ , as well as the diatomics OH, CO, SiO, CN, SO, and CS (Liszt et al. 2006, 2008).

There is remarkable overlap between the molecules found in diffuse clouds and PNe. As shown in this study, HCO^+ and CS are common constituents of PNe, and other observations have demonstrated that HCN, HNC, CCH, CN, H_2CO , SiO, and SO are prevalent in at least some PNe, as well (Bachiller et al. 1997; Tenenbaum et al. 2009; Zack & Ziurys 2013; Edwards & Ziurys 2013). The additional species H_2S , HCS^+ , and NH_3 simply have not yet been seriously searched for in these objects, to our knowledge, although Zhang et al. (2008) tentatively claim a detection of HCS^+ in NGC 7027. A comparison of CS and HCO^+ abundances found in the two types of sources support this notion. Typical abundances of CS and HCO^+ in diffuse clouds are $\sim 2.5 \times 10^{-9}$ and $\sim 2\text{--}3 \times 10^{-9}$, respectively (Liszt et al. 2006). These values are about an order of magnitude less than those found in PNe studied here, consistent with slow dispersion of the dense nebular knots of molecules and dust into the diffuse ISM as pressure equilibrium ceases. Polyatomic molecular material from PNe thus appears to be passed on to diffuse clouds.

6. CONCLUSION

PNe contribute about 85% of the matter that composes the ISM. Yet it is difficult to account for the mass of the progenitor stars in these objects in the remaining white dwarf and ionized envelope material. Molecules and dust may contain the “missing” matter. This study of five PNe, covering an evolutionary track of almost 10,000 yr, has shown that the abundances of CS and HCO⁺ do not appear to significantly decrease with nebular age. It has also shown that CS is a common constituent of PNe that have O ≥ C. The abundances measured here are consistent with slow dissipation of the dense molecular material into the diffuse ISM, seeding low density clouds with polyatomic molecules. A better understanding of the molecular content of PNe is clearly necessary in evaluating the overall chemical evolution of the ISM.

This research was supported by NSF grants AST-1140030 and AST-1211502. The Kitt Peak 12 m and the SMT are operated by the Arizona Radio Observatory (ARO), Steward Observatory, University of Arizona, with support through the NSF University Radio Observatories program (URO: AST-1140030).

REFERENCES

- Ali, A., Shalabiea, O. M., El-Nawawy, M. S., & Millar, T. J. 2001, *MNRAS*, **325**, 881
- Aller, L. H., Hung, S., & Feibelman, W. A. 1999, *PNAS*, **96**, 5366
- Ashley, M. C. B., & Hyland, A. R. 1988, *ApJ*, **331**, 532
- Bachiller, R., Bujarrabal, V., Martín-Pintado, J., & Gómez-González, J. 1989, *A&A*, **218**, 252
- Bachiller, R., Cox, P., Josselin, E., et al. 2000, in *ISO Beyond the Peaks: The 2nd ISO Workshop on Analytical Spectroscopy*, ed. A. Salama et al. (ESA SP-456; Noordwijk: ESA), 171
- Bachiller, R., Forveille, T., Huggins, P. J., & Cox, P. 1997, *A&A*, **324**, 1123
- Bernard-Salas, J., Pottasch, S. R., Beintama, D. A., & Wesselius, P. R. 2001, *A&A*, **367**, 949
- Corradi, R. L. M., Gonçalves, D. R., Villaver, E., et al. 2000, *ApJ*, **535**, 823
- Cox, P., Boulanger, F., Huggins, P. J., et al. 1998, *ApJL*, **495**, L23
- Cuesta, L., Phillips, J. P., & Mampaso, A. 1995, *A&A*, **304**, 475
- Davis, C. J., Smith, M. D., Stern, L., Kerr, T. H., & Chiar, J. E. 2003, *MNRAS*, **344**, 262
- Dobrinčić, M., Villaver, E., Guerrero, M. A., & Manchado, A. 2008, *AJ*, **135**, 2199
- Dorschner, J., & Henning, T. 1995, *A&ARv*, **6**, 271
- Edwards, J. L., & Ziurys, L. M. 2013, *ApJL*, **770**, L5
- Gonçalves, D. R., Mampaso, A., Corradi, R. L. M., et al. 2004, *MNRAS*, **355**, 37
- Hasegawa, T. I., & Kwok, S. 2001, *ApJ*, **562**, 824
- Hawley, S. A., & Miller, J. S. 1978, *PASP*, **90**, 39
- Henry, R. B. C., Kwitter, K. B., & Balick, B. 2004, *AJ*, **127**, 2284
- Henry, R. B. C., Kwitter, K. B., & Dufour, R. J. 1999, *ApJ*, **517**, 782
- Henry, R. B. C., Speck, A., Karakas, A. I., Ferland, G. J., & Maguire, M. 2012, *ApJ*, **749**, 61
- Hora, J. L., Latter, W. B., Smith, H. A., & Marengo, M. 2006, *ApJ*, **652**, 426
- Hua, C. T., & Louise, R. 1970, *A&A*, **9**, 448
- Huggins, P. J., Bachiller, R., Cox, P., & Forveille, T. 1996, *A&A*, **315**, 284
- Huggins, P. J., Bachiller, R., Planesas, P., Forveille, T., & Cox, P. 2005, *ApJS*, **160**, 272
- Huggins, P. J., & Healy, A. P. 1986, *MNRAS*, **220**, 33
- Josselin, E., & Bachiller, R. 2003, *A&A*, **397**, 659
- Kastner, J. H., Weintraub, D. A., Gatley, I., Merrill, K. M., & Probst, R. G. 1996, *ApJ*, **462**, 777
- Kasuga, T., Yamamura, I., & Deguchi, S. 1997, *A&A*, **320**, 575
- Kimura, R. K., Gruenwald, R., & Aleman, I. 2012, *A&A*, **541**, A112
- Kwok, S. 2000, *The Origin and Evolution of Planetary Nebulae* (Cambridge: Cambridge Univ. Press)
- Kwok, S., Chong, S.-N., Koning, N., Hua, T., & Yan, C.-H. 2008, *ApJ*, **689**, 219
- Liszt, H., & Lucas, R. 2001, *A&A*, **370**, 576
- Liszt, H. S., Lucas, R., & Pety, J. 2006, *A&A*, **448**, 253
- Liszt, H. S., Pety, J., & Lucas, R. 2008, *A&A*, **486**, 493
- Liu, X.-W., Barlow, M. J., Nguyen-Q-Rieu, et al. 1996, *A&A*, **315**, L257
- Liu, Y., Liu, X.-W., Barlow, M. J., & Luo, S.-G. 2004, *MNRAS*, **353**, 1251
- López-Martin, L., López, J. A., Esteban, C., et al. 2002, *A&A*, **388**, 652
- Lucas, R., & Liszt, H. S. 2002, *A&A*, **384**, 1054
- Lumsden, S. L., Puxley, P. J., & Hoare, M. G. 2001, *MNRAS*, **328**, 419
- Lupu, R. E., France, K., & McCandliss, S. R. 2006, *ApJ*, **644**, 981
- Manchado, A., Guerrero, M. A., Stanghellini, L., & Serra-Ricart, M. 1996, *The IAC Morphological Catalog of Northern Galactic Planetary Nebulae* (La Laguna, Spain: Instituto de Astrofísica de Canarias)
- Matsuura, M., Zijlstra, A. A., Gray, M. D., Molster, F. J., & Waters, L. B. F. M. 2005, *MNRAS*, **363**, 628
- McCandliss, S. R., France, K., Lupu, R. E., et al. 2007, *ApJ*, **659**, 1291
- Meaburn, J., Boumis, P., Christopoulou, P. E., et al. 2005, *RMxAA*, **41**, 109
- Meaburn, J., & López, J. A. 1993, *MNRAS*, **263**, 890
- Meixner, M., McCullough, P., Hartman, J., Son, M., & Speck, A. 2005, *AJ*, **130**, 1784
- O’Dell, C. R., Balick, B., Hajian, A. R., Henney, W. J., & Burkert, A. 2002, *AJ*, **123**, 3329
- O’Dell, C. R., Ferland, G. J., Henney, W. J., & Peimbert, M. 2013, *AJ*, **145**, 92
- O’Dell, C. R., Henney, W. J., & Ferland, G. J. 2005, *AJ*, **130**, 172
- O’Dell, C. R., Sabbadin, F., & Henney, W. J. 2007, *AJ*, **134**, 1679
- Papamastorakis, J., Xilouris, K. M., & Paleologou, E. V. 1993, *A&A*, **279**, 536
- Pardo, J. R., Cernicharo, J., Goicoechea, J. R., Güélin, M., & Asensio-Ramos, A. 2007, *ApJ*, **661**, 250
- Phillips, J. P., & Ramos-Larios, G. 2008, *MNRAS*, **383**, 1029
- Pickett, H. M., Poynter, R. L., Cohen, E. A., et al. 1998, *JQSRT*, **60**, 883
- Pottasch, S. R., Beintama, D. A., & Feibelman, W. A. 2000, *A&A*, **363**, 767
- Pottasch, S. R., Gilra, D. P., & Wesselius, P. R. 1982, *A&A*, **109**, 182
- Pulliam, R. L., Edwards, J. L., & Ziurys, L. M. 2011, *ApJ*, **743**, 36
- Rauch, T. 2003, *A&A*, **403**, 709
- Redman, M. P., Viti, S., Cau, P., & Williams, D. A. 2003, *MNRAS*, **345**, 1291
- Sahai, R., Morris, M. R., Werner, M. W., et al. 2012, *A&A*, **542**, L20
- Saito, M., Iwata, I., Okumura, S., Mori, A., & Yamashita, T. 1999, *PASJ*, **51**, 673
- Speck, A. K., Meixner, M., Fong, D., et al. 2002, *AJ*, **123**, 346
- Speck, A. K., Meixner, M., Jacoby, G. H., & Knezek, P. M. 2003, *PASP*, **115**, 170
- Sterling, N. C., & Dinerstein, H. L. 2008, *ApJS*, **174**, 158
- Tajitsu, A., & Tamura, S. 1998, *AJ*, **115**, 1989
- Tenenbaum, E. D., Dodd, J. L., Milam, S. N., Woolf, N. J., & Ziurys, L. M. 2010, *ApJS*, **190**, 348
- Tenenbaum, E. D., Milam, S. N., Woolf, N. J., & Ziurys, L. M. 2009, *ApJL*, **704**, L108
- Turner, B. E. 1991, *ApJS*, **76**, 617
- van der Tak, F. F. S., Black, J. H., Schöier, F. L., Jansen, D. J., & van Dishoeck, E. F. 2007, *A&A*, **468**, 627
- van Hoof, P. A. M., Van de Steene, G. C., Barlow, M. J., et al. 2010, *A&A*, **518**, L137
- Vázquez, R., López-Martin, L., Miranda, L. F., et al. 2000, *A&A*, **357**, 1031
- Woods, P. M., & Nyman, L. A. 2005, in *IAU Symp. 231, Astrochemistry throughout the Universe: Recent Successes and Current Challenges*, ed. D. C. Lis, G. A. Blake, & E. Herbst (Cambridge: Cambridge Univ. Press), 326
- Zack, L. N., & Ziurys, L. M. 2013, *ApJ*, **765**, 112
- Zeigler, N. R., Zack, L. N., Woolf, N. J., & Ziurys, L. M. 2013, *ApJ*, **778**, 16
- Zhang, Y., Kwok, S., & Dinh-V-Trung, 2008, *ApJ*, **678**, 328
- Zhang, Y., Kwok, S., & Dinh-V-Trung, 2009, *ApJ*, **691**, 1660
- Ziurys, L. M., Tenenbaum, E. D., Pulliam, R. L., Woolf, N. J., & Milam, S. N. 2009, *ApJ*, **695**, 1604
- Zuckerman, B., & Gatley, I. 1988, *ApJ*, **324**, 501